Advances in Chemical Physics
Edited by K. P. Lawley

HELIUM-SCATTERING STUDIES OF THE DYNAMICS AND PHASE TRANSITIONS OF SURFACES

KLAUS KERN and GEORGE COMSA

Institut für Grenzflächenforschung und Vakuumphysik, KFR Jülich, P.O. Box 1913, D-5170 Jülich, Federal Republic of Germany

CONTENTS

1. INTRODUCTION

The access to the bulk of a solid is obviously through the surface. In spite of this, we know much more about the properties of the three-dimensional (3D) bulk than about the two-dimensional (2D) surfaces. One of the main reasons – from the experimentalist's point of view – is the relatively small number of surface atoms. As a consequence, the interaction cross-section of the probe particles with the surface atoms has to be large enough but, at the same time, the interaction should not disturb too much the sampled object. These conditions can be certainly contradictory. The most widespread surface probe is the electron. The overwhelming part of our present knowledge about surfaces is due to the use of electron beams as probe, as information carrier and as both. Even in domains for which they do not seem to be particularly appropriate, like phase transitions of physisorbed layers and low energy phonons, electron based methods have supplied valuable information. A remarkable effort had to be made for these achievements: the energy resolution had to be pushed to its limits and the disturbing effect of the electrons on the investigated phases – which are by definition particularly delicate near transitions – has always to be accounted for. In contrast, at least for these domains of investigation, the He atom seems to be the natural probe. Due to its large mass, the He atom has the right wavelength (~ 1 Å) for structural studies of surface phases at thermal energies. He atoms at these energies have two outstanding properties: they do not disturb the surface in any way and they are absolutely surface sensitive. In addition, they are extremely sensitive with respect to surface disorder; this allows the detailed characterization of surface disorder, which is always present even on the best prepared surfaces and which plays an important role in phase formation and transition. Due again to their large mass, the He atoms have, like the neutrons, a favorable relationship between momentum and energy: the momentum of He atoms is large enough to create a phonon anywhere in the Brillouin zone already at kinetic energies of the same order with the energy transferred. Accordingly, the energy resolution can be high enough for a detailed monitoring of dispersion curves and even for lifetime broadenings of characteristic energy exchange peaks. The analogy with the capabilities of thermal neutrons, which have allowed an almost complete understanding of the dynamics of the 3D bulk of solids, suggests that the use of thermal He-scattering will lead to comparable results for the 2D surfaces.

After discussing specific, basic and experimental aspects of the use of thermal He as a surface probe we will review recent results obtained in the study of surface dynamics and of 2D phase transitions.

2. THERMAL HE-BEAM SCATTERING AT SURFACES

The structural and dynamical properties of solid surfaces at atomic level are conveniently derived from scattering experiments. Thermal neutrons, X-ray photons, low energy electrons or thermal He atoms can be chosen as probes. Neutrons and X-rays interact weakly with the sample atoms. This is advantageous because the structural information is obtained within the straightforward kinematical approximation; it has, however, the disadvantage that these probe particles are basically surface insensitive. Surface sensitivity can only be obtained by using grazing angles of incidence (X-rays) or by using substrates with large surface-to-bulk ratio like powder samples (neutrons). On the other hand, electrons and He atoms have stronger scattering interactions which complicate in general the structural analysis, but which also ensure an

TABLE 1
Characteristics of the various surface probe particles.

Properties	Probe particles			
	He atoms	Electrons	Neutrons	X-ray photons
Energy (meV)	$5–10^2$	$10^4–3 \times 10^5$	$1–10^2$	$4 \times 10^6–3 \times 10^7$
Wavelength–energy relation (λ in Å, E in meV)	$\lambda = \frac{4.54}{\sqrt{E}}$	$\lambda = \frac{389}{\sqrt{E}}$	$\lambda = \frac{9.04}{\sqrt{E}}$	$\lambda = \frac{12.39 \times 10^8}{\sqrt{E}}$
Information depth (number of layers)	1	3–5	$\gg 1$	$\gg 1$
Energy resolution (meV)	0.2	3	0.001	> 8
Momentum resolution ($Å^{-1}$)	10^{-2}	10^{-2}	$10^{-2}–10^{-3}$	10^{-4}
Sample	single crystal	single crystal	powder	single crystal powder
Maximum ambient pressure (Pa)	10^{-3}	10^{-3}	$> 10^5$	$> 10^5$

information depth confined to a few layers (electrons) or to the outermost surface layer only (He atoms).

In Table 1 we give the main parameters which characterize the surface analytical properties of the various probe particles.

2.1. He atoms as probe particles

It is primarily the exclusive surface sensitivity of thermal atom scattering which makes this method to an outstanding surface probe. This was recognized more than sixty years ago by T. H. Johnson[1]:

'These experiments are of interest not only because of their confirmation of the predictions of quantum mechanics, but also because they introduce the possibility of applying atom diffraction to investigations of the atomic constitution of surfaces. A beam of atomic hydrogen, for example, with ordinary thermal velocities, has a range of wavelengths of the right magnitude for this purpose, centering aroung 1 Å, and the complete absence of penetration of these waves will insure that the effects observed arise entirely from the outermost atomic layer'.

In spite of this early recognition of the potential provided by thermal atoms to study surfaces, the lack of an appropriate He-beam source was the main hurdle in the development of this now very powerful analytical tool. For a long time the Knudsen (effusion) cell was the only means for producing molecular beams. The Maxwellian effusive beams have low intensity ($I_0 \sim 10^{14}$ particles $s^{-1}sr^{-1}$) and low monochromaticity ($\Delta v/v = \Delta\lambda/\lambda = 0.95$). Monochromaticity improvement by means of mechanical velocity selectors reduces the already low intensity to a level which in view of the inefficient He detection is unacceptable for a decent analysis. The major breakthrough has been the development of high pressure nozzle sources. The effect achieved by the invention of these sources is only comparable to that of laser technology: simultaneous increase of intensity and monochromaticity by several orders of magnitude. Indeed, intensities of 10^{19} particles $s^{-1}sr^{-1}$ and monochromaticities of $\Delta v/v = \Delta\lambda/\lambda \approx 0.01$ are obtained routinely today.

The nautre of the He–surface interaction potential determines the major characteristics of the He beam as surface analytical tool. At larger distances the He atom is weakly attracted due to dispersion forces. At a closer approach, the electronic densities of the He atom and of the surface atoms overlap, giving rise to a steep repulsion. The classical turning point for thermal He is a few angstroms in front of the outermost surface layer. This makes the He atom sensitive exclusively to the outermost layer. The low energy of the He atoms and their inert nature ensures that He scattering is a completely non-destructive surface probe. This is particularly important when delicate phases, like physisorbed layers, are investigated.

The de Broglie wavelength of thermal He atoms is comparable with the interatomic distances of surfaces and adsorbed layers. Thus, from measurements of the angular positions of the diffraction peaks the size and orientation of the 2D unit cell, i.e. the structure of the outermost layer, can be straightforwardly determined. Analysis of the peak intensities yields the potential corrugation, which usually reflects the geometrical arrangement of the atoms within the 2D unit cell[2].

The energy of thermal He atoms is comparable with the energy of collective excitations (phonons) of surfaces and overlayers. Thus, in a scattering experiment the He atom may exchange an appreciable part of its energy with the surface. This energy can be measured in time-of-flight experiments with a resolution ~ 0.2 meV; the resolution can be brought even to ~ 0.1 meV (when using very low beam energies, $\simeq 8$ meV). Thus, surface phonon dispersion curves can be mapped out by measuring energy loss spectra at various momentum transfers in definite crystallographic directions. This is a substantial advantange of inelastic He scattering over inelastic neutron scattering. (In view of the random orientation of powdered samples, which have to be used in neutron scattering, only average phonon density of states, but not dispersion curves, can be obtained.) The range of energy transfer that can be covered by thermal He atoms is limited at the low end by the present maximum resolution of ~ 0.1 meV and at the high end by the nature of the scattering mechanism. The interaction time of thermal He atoms with the surface being larger than 10^{-13} s, the upper limit for the observable phonon modes is about 40 meV. From this point of view high resolution electron scattering is more advantageous. So far only modes with a large component perpendicular to the surface have been clearly detected; this seems to be less a fundamental, but rather a technical problem.

Besides the inelastic component, always a certain number of He atoms are elastically scattered in directions lying between the coherent diffraction peaks. We will refer to this scattering as diffuse elastic scattering. This diffuse intensity is attributed to scattering from defects and impurities. Accordingly, it provides information on the degree and nature of surface disorder. It can be used for example to study the growth of thin films[3] or to deduce information on the size, nature and orientation of surface defects[4]. Very recently from the analysis of the diffuse elastic peak width, information on the diffusive motion of surface atoms has been obtained[5].

Another remarkable way to use He scattering for the study of adsorbed layers is based on the large total cross-section Σ for diffuse He scattering of isolated adsorbates (e.g. $\Sigma > 100$ Å^2 for a number of adsorbates like Xe, CO, NO; and even for H, $\Sigma > 20$ Å^2). This large cross-section is attributed to the long range attractive interaction between adatom and the incident He atom, which causes the He atoms to be scattered out of the coherent beams. The remarkable size of the cross-section allows the extraction of important

information concerning the lateral distribution of adsorbates, mutual interactions between adsorbates, dilute–condensed phase transitions in 2D, adatom mobilities, etc.[6], simply by monitoring the attenuation of one of the coherently scattered beams, in particular of the specular beam. This technique also allows the detection of impurities (including hydrogen!) in the permill range, a level hardly attainable with almost all other methods. For a detailed discussion of the application of this He scattering mode we refer to Ref. 6.

2.2. Experimental aspects

Like all analytical methods, the thermal He-scattering device can be represented schematically as in Fig. 1. It consists mainly of a source and a detector. The high pressure nozzle source provides a highly monochromatized flux of thermal He atoms which is then collimated to a narrow beam of thermal He atoms. This well-defined flux of probe particles impinges on the sample at a polar angle ϑ_i and azimuthal angle φ_i. The detector measures the properties of the He atoms which, after interacting with the sample, serve as information carriers. By determination of the whole set of spatial and energetic distributions of the scattered He atoms, the double differential scattering cross-section, containing the whole set of structural and dynamical information, can be determined. In contrast to electron spectrometers, where either the elastic or the inelastic scattering cross-section are measured in order to obtain structural information (LEED) or dynamical information (EELS), respectively, the currently operated high resolution He scattering spectrometers are hybrids. They are designed to measure structural and dynamical surface properties in one experiment, i.e. designed to measure the double differential scattering cross-section. This duality is achieved at the expense of very high diffraction capabilities. The instrumental transfer width, i.e. the momentum resolution of a He diffractometer, is governed by the angular spread of the He beam and of the detector and by the monochromaticity of the He wave. The now available primary He beam intensities are large enough to allow the

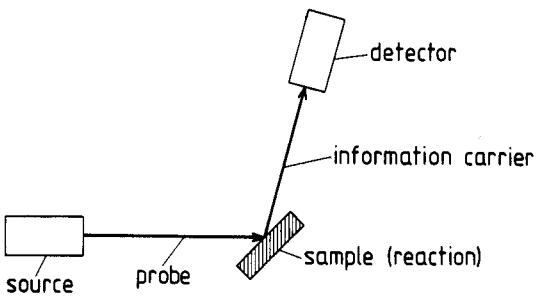

Fig. 1. Schematic of a surface scattering experiment.

construction of He diffractometers with transfer widths of several thousand angstroms, by monochromatizing the primary He beam (e.g. with Fizeau selectors) and by reducing the limiting apertures. This transfer width size is comparable to that of synchrotron X-ray diffractometers. However, in view of the low probability for the excitation of surface short wavelength phonons a compromise has to be found when building a hybrid spectrometer. This results in transfer widths of a few hundred angstroms, which are still larger than in conventional LEED systems.

The highly monochromatic He beam source is a nozzle beam generator which has been described in detail in Refs. 7 and 8. In brief, the monochromatic He beam is produced by expanding extra-high-purity helium from a high pressure reservoir (150 bar) through a narrow nozzle orifice (5 μm) into a chamber which is evacuated by a 1500 l s^{-1} turbomolecular pump boostered by a 150 m^3 h^{-1} roots blower. During expansion the translational energy distribution of the gas sharpens by about two orders of magnitude; the beam flux energy becomes $E_{He} = \frac{5}{2}kT_0$, i.e. 20% larger than the flux energy of an effusion beam from a reservoir at the same temperature, T_0. By varying the nozzle temperature, T_0, beam energies in the range 100 meV ($\lambda = 0.45$ Å) to 5 meV ($\lambda = 2.03$ Å) are easily obtained. Cooling the source with liquid nitrogen (which leads here to an effective nozzle temperature of $T_0 = 85$ K) results in a 18.3 meV beam with an energy width of 0.25 meV (FWHM) and an intensity of $\sim 2 \times 10^{19}$ He atoms s^{-1} sr^{-1}. Upon expansion, the collimation is obtained by a skimmer and one or two subsequent apertures separating differentially pumped chambers.

The major problems in high resolution He scattering are connected with the detection: large background and low detection efficiency. While with some technical effort the background can be efficiently reduced, no real breakthrough has been so far achieved in the attempt to increase the detection efficiency of He beams without impairing the time resolution. The method of choice is still electron bombardment ionization, followed by ion mass analysis. The real detection efficiency hardly surpasses 10^{-6}, while the time resolution is fully sufficient for time-of-flight He velocity analysis. Recent attempts to monitor the He metastables (generated also by electron bombardment) instead of He ions may be advantageous, when the He background pressure in the detector can not be made low enough. In this type of detection, the relatively lower efficiency is compensated by a favorable directionality effect: the He atoms in the beam are more efficiently detected than those in the isotropic background.

A relatively high He background is obviously inherent in all He-beam experiments. Even a highly collimated beam puts a continuous, heavy He load on the pumps evacuating the sample chamber. In the case of the apparatus shown in Fig. 2, the beam collimated to 0.2° (1.5×10^{-6} sr) supplies the sample chamber with about 1.5×10^{13} He/sec (5.7×10^{-7} mbar l/s). In view of some

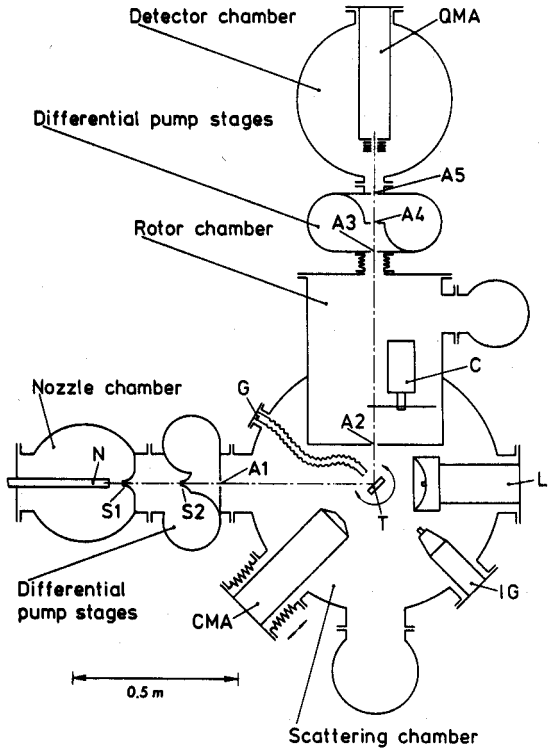

Fig. 2. Schematic diagram of a high resolution He time-of-flight spectrometer. N – nozzle beam source, S1, 2 – skimmers, A1–5 – apertures, T – sample, G – gas doser, CMA – Auger Spectrometer, IG – ion gun, L – LEED, C – magnetically suspended pseudorandom chopper, QMA – detector, quadrupole mass analyzer with channeltron.

additional He load from the beam generator system and with a reasonably sized pumping system, the He background level in the sample chamber is rarely below 10^{-9} mbar. A detector located in this chamber would have a dynamical range of $\sim 10^2$–10^3. This is acceptable when the information is inferred from the intense specular beam, but out of question when diffraction patterns of adlayers or inelastic scattering spectra are sought. The only practical way for a radical background reduction is the differential pumping. In the example in Fig. 2, the scattering (sample) chamber is separated by three differential pumping chambers (one of them contains the chopper) which, together with the very efficient (high compression ratio) pumping of the detector chamber, leads to a He background pressure of $\sim 10^{-15}$ mbar in the latter. This results in an effective dynamical range of $\sim 10^6$. Very low intensity diffraction peaks (like second-order diffraction peaks from clean packed metal

surfaces) or weak inelastic resonances can be clearly resolved out of the background.

The total of eight individually pumped chambers separated by small orifices keeps a pressure ratio of 20 orders of magnitude between the He source reservoir and detector. This is done at the expense of the flexibility of the scattering geometry. In the case of the apparatus shown in Fig. 2, the angle between incident and outgoing beam is fixed at $\vartheta_i + \vartheta_f = 90°$.

The UHV sample chamber has a base pressure in the low 10^{-11} mbar range. The chamber contains conventional crystal cleaning (ion sputter gun) and analyzing devices (LEED, CMA–Auger). Special emphasis has been put on the design of the sample holder, because the fixed scattering geometry requires the diffraction scans to be made by rotations of the crystal. In Ref. 8 we have described in detail a sample holder which allows independent polar and azimuthal rotation as well as tilt with the sample temperature continuously adjustable between 25 K and 1800 K. Recently we have improved the cooling device of the sample holder, allowing now for temperatures as low as 15 K. Both the polar and azimuthal angles are varied by step motors. This ensures a continuous and accurate scanning, which is essential when monitoring diffraction scans. The step motors and the transmission used here allow an angular resolution of the polar and azimuthal sample rotation of 0.018° and 0.009°, respectively.

The velocity distribution of atoms scattered from a surface is usually determined by measuring the time they need to cover a given distance (the so-called time-of-flight (TOF) method). The flight path is defined by the position of the chopper blade, which is placed between sample and detector, and the center of the electron beam bombardment ionizer. For a maximal resolution the chopper opening function (gate function) should be in the ideal case a δ-function. In Fig. 3 the gate function and the TOF distribution of a 18 meV He nozzle beam are shown schematically. The time interval between gate

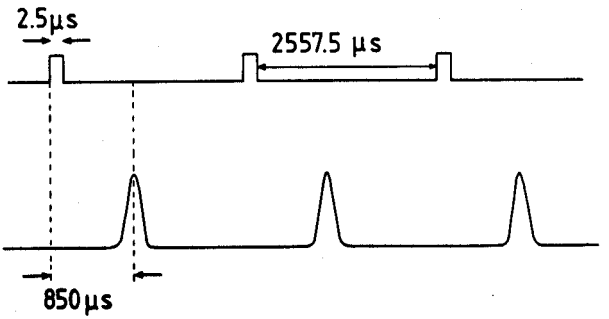

Fig. 3. Gate function and the TOF distribution of He atoms from an 18 meV nozzle beam (flight path 790 mm).

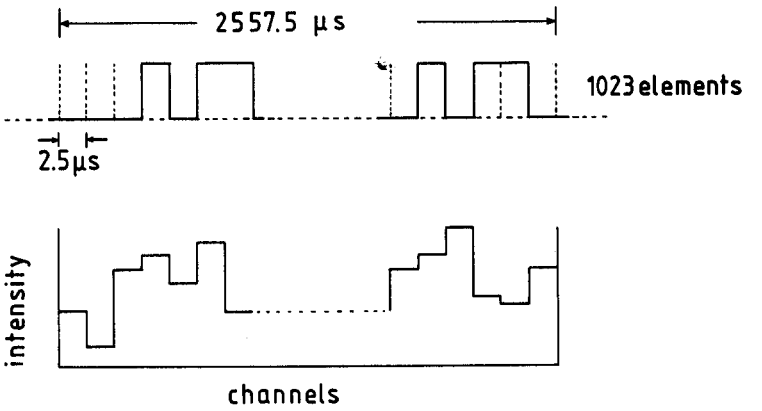

Fig. 4. Gate function of a pseudorandom sequence of slots and bars and a schematic intensity distribution.

openings has to be large enough so that superpositions of slow and rapid atoms originating from successive openings can be neglected. The transmission is equal to the ratio between gate opening time and the interval between openings. Thus the width of the gate function, i.e. the time resolution, is a compromise between the ideal δ-function and an acceptable transmission. The compromise shown in Fig. 3 results in a resolution of about 0.3% with respect to the average TOF and a rather low transmission of 0.1%. In view of the signal-to-noise problems due to the background this transmission is unsatisfactory.

An elegant and efficient alternative is the use of pseudorandom chopping. This method was first introduced in inelastic neutron scattering studies in the late 1960s. The gate function is a 'pseudorandom' sequence of slots and bars (Fig. 4, upper part). We use here a binary shift register sequence of 512 slots and 511 bars, of 2.5 μs width each (at a rotor speed of 391 Hz). The distribution of arrival times (Fig. 4, lower part) is deconvoluted to the TOF distribution by cross-correlation. A detailed description of the pseudorandom TOF technique can be found in Refs. 9–11. The transmission is close to 50%, independent of time resolution. The severe requirement of a highly constant rotation period of the chopper during the whole measuring time and a very low phase jitter (smooth rotation) of the chopper during each revolution is difficult to satisfy under UHV conditions. This has been realized here by using a magnetically suspended chopper.

A matter of controversial discussion is the comparison of pseudorandom and conventional single slot chopping; for details see Ref. 11. The comparison can be expressed quantitatively by introducing the gain factor $G(f_k)$, which represents the ratio of the variances resulting in channel k from the two kinds

of chopping. For binary shift register sequences, the gain factor is given by

$$G(f_k) = \frac{\sigma^2 \text{ single slot}}{\sigma^2 \text{ pseudorandom}} \simeq \frac{1}{2}\frac{f_k + \bar{u}}{\bar{f} + \bar{u}/n}, \tag{1}$$

where f_k is the number of counts of the time-dependent signal in channel k, $\bar{f}$ is its mean value, $\bar{u}$ is the mean number of counts per channel of the time-independent signal (the real background), and n the number of slots of the pseudorandom sequence. The pseudorandom chopping has to be preferred when $G(f_k) > 1$. This is always the case when $\bar{u} > 2\bar{f}$ because $n \gg 1$. The general interest, so far, is focussed on the position, height, and shape of the peaks in the TOF spectra and much less on the shape of a possibly present energy-dependent background. In this case a much less restrictive condition can be deduced: the pseudorandom chopping has to be preferred when in the 'interesting' channels $f_k > 2\bar{f}$, irrespective of the value of $\bar{u}$. This condition is fulfilled for all significant peaks and thus the pseudorandom chopping is of advantage, even if technically more demanding.

The effective resolution of the He scattering spectrometer as a whole is in fact the figure of primary interest. For the spectrometer used in the authors' laboratory the effective resolution function of the chopper, taking into account the finite width of the beam, of the chopper slots and of the channels, has a full width at half-maximum (FWHM) of ~ 1.27 times the width of one chopper slot, i.e. 3.2 μs. Together with the velocity spread of the beam generated by the source ($\sim 0.7\%$ FWHM) and the finite length of the ionization region (estimated as ~ 5 mm FWHM) the overall instrumental resolution amounts to $\sim 8\,\mu$s FWHM for a typical flight time of 800 μs corresponding to 0.40 meV FWHM at 20 meV beam energy. These values are in agreement with the experimental width of the elastic peaks (specular and diffuse elastic) in the energy spectra taken from a clean Pt(111) surface.

3. SURFACE DYNAMICS

3.1. Some basic lattice dynamics

3.1.1. Surface phonons

This section deals with the dynamics of collective surface vibrational excitations, i.e. with surface phonons. A surface phonon is defined as a localized vibrational excitation of a semi-infinite crystal, with an amplitude which has wavelike characteristics parallel to the surface and decays exponentially into the bulk, perpendicular to the surface. This behavior is directly linked to the broken translational invariance at a surface, the translational symmetry being confined here to the directions parallel to the surface.

The phonon spectrum of a crystal surface consists of two parts. The bulk

bands, which are due to the projection of bulk phonons onto the two-dimensional Brillouin zone of the particular surface, and the specific surface phonon branches which are due to the broken translational invariance. This is exemplified in Fig. 5 for a close-packed (111) surface of a face-centered cubic crystal. The theoretical dispersion curves have been calculated by Allen *et al.*[12] Already in 1971, they analyzed the vibrational spectra of low index surfaces of f.c.c. crystals in the quasiharmonic approximation using Lennard–Jones pair

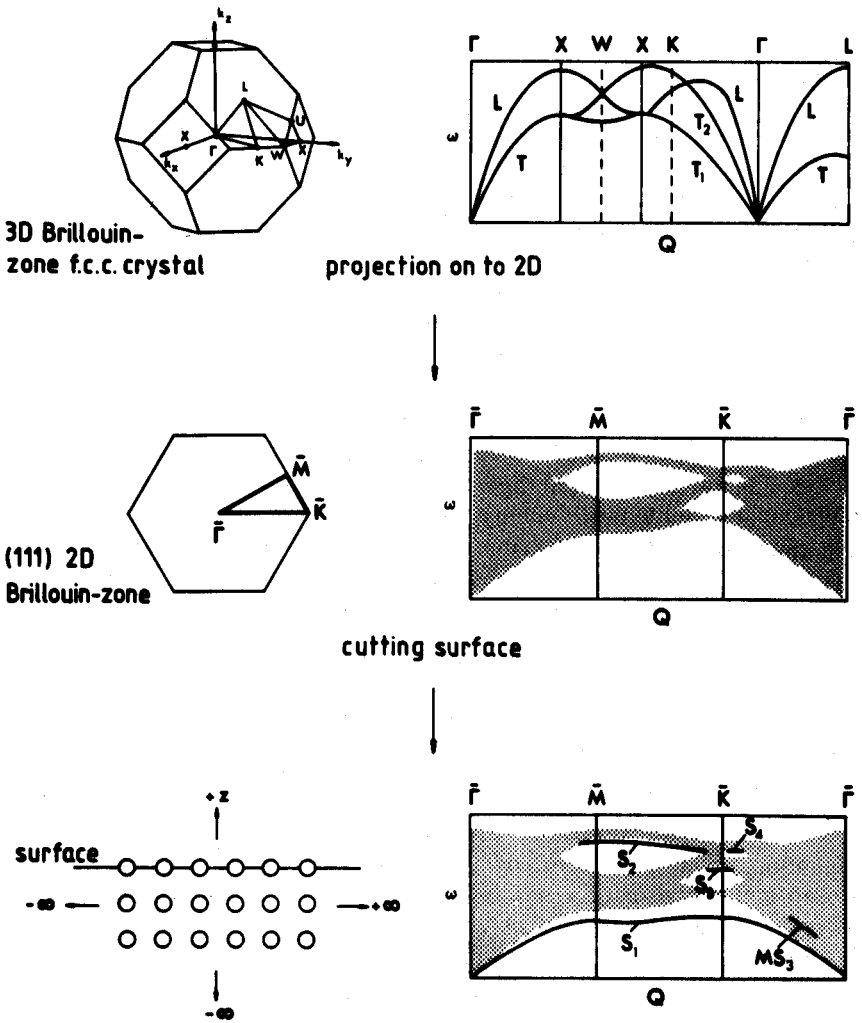

Fig. 5. Schematics of the formation of the surface phonon dispersion of a (111) f.c.c. crystal.

potentials. The solid lines, termed S_1–S_4, are specific surface phonon branches. These true surface modes only exist outside or in gaps of the projected bulk phonon bands of equivalent symmetry. However, inside the bulk bands there may exist well-defined modes with maximum amplitudes in the surface layer, but non-vanishing amplitudes in the bulk. Mode MS_3 in Fig. 5 is an example of such a 'surface resonance'. Of particular interest is the lowest frequency mode below the transverse bulk band edge. In this mode, the atoms are preferentially vibrating in the plane defined by the surface normal and the propagation direction, i.e. in the sagittal plane. This wave is called the Rayleigh wave.

Surface waves are usually discussed in two limits. Phonons whose wavelength is much larger than the atomic spacing of the crystal can be treated in the continuum limit, i.e. the elastic response of the crystal surface can be described in terms of average interatomic forces. When the ratio of wavelength and atom spacing is smaller than, say ~ 100, this approximation is no longer justified. The forces between the atoms have now to be taken into account in detail. This is the reason why the short wavelength phonons are of primary interest to surface physicists. The surface phonon dispersion directly reflects the interatomic force field at the surface.

3.1.2. Continuum limit

It was Lord Rayleigh[13] who was first to derive the dispersion relations for surface acoustic waves propagating along the surface of an isotropic elastic continuum with a planar, stress-free surface. Phonons are called acoustic when the frequency goes to zero for diverging wavelengths, otherwise they are called optic. The frequency ω_R of the Rayleigh wave varies linearly with wave vector $Q_\parallel$, the proportionality constant being the speed of sound c_R at the surface:

$$\omega_R = c_R Q_\parallel \tag{2}$$

The Rayleigh wave speed of sound c_R is determined by the equation:

$$[(K+2\mu)/\mu]\left[\left(\frac{c_R^2}{c_t^2}\right)^3 - 8\left(\frac{c_R^2}{c_t^2}\right)^2 + 8\left(\frac{3c_t^2}{c_l^2} - 2\right)\right] + 16\left(1 - \frac{c_t^2}{c_l^2}\right) = 0 \tag{3}$$

with $c_R/c_t < 1$ and K, μ being the Lamé coefficients of an elastic body. Here, c_t and c_l are the transverse and longitudinal sound velocities of the bulk, respectively. Resonable values for the ratio c_R/c_t range from 0.96 (non-compressible solids) to 0.69 (limit of stability for an elastic body). The displacement pattern of the Rayleigh wave is described by ellipsoids in the sagittal plane. The decay length of the amplitudes into the elastic bulk is of the order of the wavelength $\lambda = (2\pi/Q_\parallel)$. In Fig. 6 we show the displacement pattern and the decay length of a square lattice given by Farnell[14].

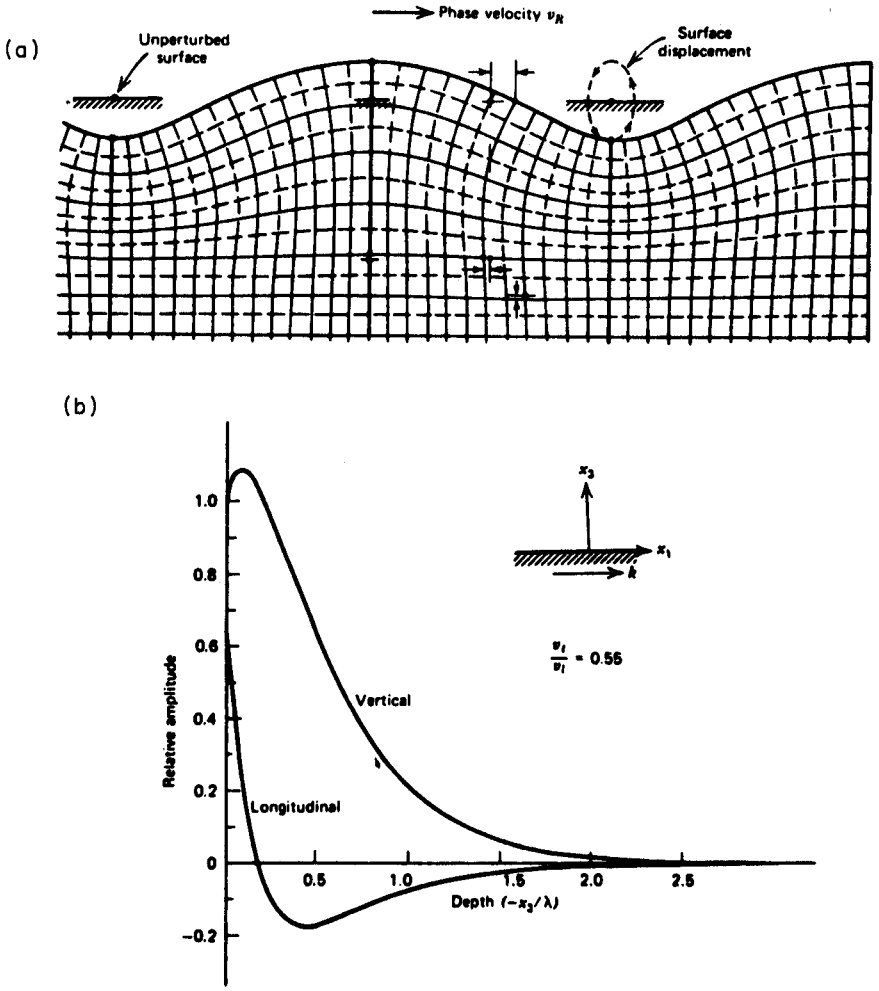

Fig. 6. (a) Distortion of a square lattice in a plane containing the surface normal and the propagation direction of the Rayleigh wave. (*After Ref. 14.*). (b) Relative amplitudes of the vertical and longitudinal displacements of the Rayleigh wave as a function of penetration depth into the bulk. (*After Ref. 14.*)

3.1.3. Lattice dynamics

The dispersion curves of surface phonons of short wavelength are calculated by lattice dynamical methods. First, the equations of motion of the lattice atoms are set up in terms of the potential energy of the lattice. We assume that the potential energy φ can be expressed as a function of the atomic positions $\vec{R}(\vec{l}_{\parallel}, l_z)$ in the semi-infinite crystal. The location of the nth atom can be

written:

$$\vec{R}(\vec{l}_{\parallel}, l_z) = \vec{R}_0(\vec{l}_{\parallel}, l_z) + \vec{u}(\vec{l}_{\parallel}, l_z) \tag{4}$$

The vector $\vec{l}_{\parallel}$ specifies the position of the atom in a two-dimensional lattice in a plane parallel to the surface and the value of l_z identifies the lattice plane with respect to the surface ($l_z = 1$ for the surface layer. $\vec{u}$ is the displacement of the vibrating atom from its equilibrium position $\vec{R}_0$. The total kinetic energy of the vibrating lattice is

$$T = \frac{1}{2} \sum_{\vec{l}_{\parallel}, l_z, \alpha} m(\vec{l}_{\parallel}, l_z) \dot{u}_{\alpha}^2(\vec{l}_{\parallel}, l_z) \tag{5}$$

with m being the mass of the particular atom and α indexing the Cartesian coordinates of $\vec{u}$. For small displacements, we may expand the potential energy in a Taylor series:

$$\varphi = \varphi_0 + \sum_{\vec{l}_{\parallel}, l_z, \alpha} \Phi_{\alpha}(\vec{l}_{\parallel}, l_z) u_{\alpha}(\vec{l}_{\parallel}, l_z) + \frac{1}{2} \sum_{\vec{l}_{\parallel}, l_z, \alpha} \sum_{\vec{l}_{\parallel}, l_z, \beta} \times \Phi_{\alpha\beta}(\vec{l}_{\parallel}, l_z; \vec{l}'_{\parallel}, l'_z) u_{\alpha}(\vec{l}_{\parallel}, l_z) u_{\beta}(\vec{l}'_{\parallel}, l'_z) \tag{6}$$

with

$$\Phi_{\alpha}(\vec{l}_{\parallel}, l_z) = \left. \frac{\partial \phi}{\partial u_{\alpha}(\vec{l}_{\parallel}, l_z)} \right|_{u=0}$$

$$\Phi_{\alpha\beta}(\vec{l}_{\parallel}, l_z; \vec{l}'_{\parallel}, l'_z) = \left. \frac{\partial^2 \phi}{\partial u_{\alpha}(\vec{l}_{\parallel}, l_z) \partial u_{\beta}(\vec{l}'_{\parallel}, l'_z)} \right|_{u=0}$$

being the first and second derivatives of the potential evaluated at the equilibrium positions. In the harmonic approximation only terms up to the second order are retained. The negative gradient $-\partial\phi/\partial u_{\alpha}(\vec{l}_{\parallel}, l_z)$ is the force, acting on the lattice atom $(\vec{l}_{\parallel}, l_z)$ in direction α. When all atoms are at their equilibrium sites they experience no force by definition and we have:

$$\Phi_{\alpha}(\vec{l}_{\parallel}, l_z) = 0, \qquad \sum_{\vec{l}_{\parallel}, \vec{l}'_{\cdot}} \Phi_{\alpha\beta}(\vec{l}_{\parallel}, l_z; \vec{l}'_{\parallel}, l'_z) = 0 \tag{7}$$

In the framework of the Euler–Lagrange formalism, we write the equation of motion for the displacements of the atoms as:

$$M(\vec{l}_{\parallel}, l_z) \ddot{u}_{\alpha}(\vec{l}_{\parallel}, l_z) = - \sum_{\vec{l}_{\parallel}, l_z, \beta} \Phi_{\alpha\beta}(\vec{l}_{\parallel}, l_z; \vec{l}'_{\parallel}, l'_z) u_{\beta}(l'_{\parallel}, l'_z) \tag{8}$$

We take advantage of the translational symmetry parallel to the surface by seeking solutions to Eq. (8) of the form

$$u_{\alpha}(l_{\parallel}, l_z) = \sqrt{M(\vec{l}_{\parallel}, l_z)} u_{\alpha}(\vec{Q}_{\parallel}; l_z) \exp(i\vec{Q}_{\parallel} \vec{R}_0(\vec{l}_{\parallel}, l_z) - i\omega t) \tag{9}$$

with $\vec{Q}_{\parallel}$ being a wave vector parallel to the surface. If Eq. (9) is substituted into Eq. (8) we obtain a set of linear equations in the amplitudes

$w_\alpha(\vec{Q}_\parallel; l_z) = \sqrt{M(\vec{l}_\parallel, l_z)}u_\alpha(\vec{Q}_\parallel; l_z)$:

$$\omega^2 w_\alpha(\vec{Q}_\parallel; l_z) = \sum_{l'_z,\beta} D_{\alpha\beta}(\vec{Q}_\parallel; l_z, l'_z) w_\beta(\vec{Q}_\parallel; l'_z) \tag{10}$$

with the dynamical matrix:

$$D_{\alpha\beta}(\vec{Q}_\parallel, l_z, l'_z) = \sum_{\vec{l}'_\parallel} [\Phi_{\alpha\beta}(\vec{l}_\parallel, l_z; l'_\parallel, l_z)/\sqrt{M(\vec{l}_\parallel, l_z)M(\vec{l}'_\parallel, l'_z)}] \times \exp[i\vec{Q}_\parallel(\vec{R}_0(\vec{l}'_\parallel, l'_z) - \vec{R}_0(\vec{l}_\parallel, l_z))] \tag{11}$$

The sum $D_{\alpha\beta}$ is called the partially Fourier transformed dynamical matrix, which depends only on $\vec{Q}_\parallel$, l'_z and l_z. For each wave vector $\vec{Q}_\parallel$ the normal mode frequencies of the crystal can be found by setting the secular determinant equal to zero:

$$|D_{\alpha\beta}(\vec{Q}_\parallel; l_z, l'_z) - \omega^2 \delta_{\alpha\beta}\delta_{l_z,l'_z}| = 0 \tag{12}$$

Due to the hermitian character of the dynamical matrix, the eigenvalues are real and the eigenvector satisfies the orthonormality and closure conditions.

The coupling coefficients $\Phi_{\alpha\beta}$ are given by

$$\Phi(ij) = \delta_{ij} \sum_{j' \neq i} K_{\alpha\beta}(ij') - (1 - \delta_{ij}) K_{\alpha\beta}(ij) \tag{13a}$$

with

$$K_{\alpha\beta}(ij) = \frac{\Phi'_{ij}}{|\vec{r}_i - \vec{r}_j|}\delta_{\alpha\beta} + \left(\Phi''_{ij} - \frac{\Phi'_{ij}}{|\vec{r}_i - \vec{r}_j|}\right) n_\alpha(ij) n_\beta(ij) \tag{13b}$$

where Φ'_{ij} and Φ''_{ij} are the first and second derivatives of the two-body potential connecting atom i and j and $n_\alpha(ij)$ the αth Cartesian component of a unit vector pointing from atom i to atom j.

The solution of Eq. (12) provides the dispersion curves of the surface phonons. However, this solution requires the knowledge of the coupling constants Φ''_{ij} in the bulk and at the surface. The determination of the coupling constants can be done in several ways. The most direct way, but also the most difficult way, is the *ab initio* calculation of the electronic ground state energy as a function of the displacement of the atom cores; the second derivative of the energy with respect to the displacements provides the force constants. So far, this method has only been used to evaluate the surface phonon dispersion of low index Al surfaces[15]. The most common way to obtain coupling parameters, however, is to fit the data with calculated dispersion curves, with the force constants of surface atoms (intra- and interlayer force constants) as fitting parameters. The surface constants can obviously differ from the bulk ones due to the broken translational invariance: surface atoms have less neighboring atoms than bulk atoms. The changed force field at the surface can lead to relaxation phenomena in the selvedge. Various attempts have been undertaken to elucidate the forces responsible for the surface relaxation. An

intuitive model is the point ion model of Finnis and Heine[16] based on the electron smoothing concept of Smoluchowsky[17]. This is exemplified in Fig. 7. The electrons have the tendency to spill over the surface in order to create a geometrically smooth surface and thus lower their kinetic energy. The new electron distribution causes electrostatic forces on the ion cores of the surface atoms, resulting in an inward relaxation of the first layer. The Finnis and Heine model is certainly too simple to be more than qualitatively correct. However, there is still interest in improving the model by more sophisticated electron density distributions and accounting for electron screening of the ion motion[18].

It would be most desirable to have a direct link between the geometrical relaxations and the force constant changes. From molecular vibrational spectroscopy it is well known that the intramolecular force constants show a scaling behavior, Badger's rule[19]:

$$\Phi''_{ij} = \Phi''_b (r_b / r_{ij})^{\alpha} \tag{14}$$

with r_{ij} being the distance between atom i and j and r_b nearest neighbor distance in equilibrium.

Recently, Baddorf *et al.* have studied the removal of the relaxation of the Cu(110) surface at 100 K upon hydrogen adsorption[20]. It is well established that the (110) surfaces of face-centered cubic metals exhibit large oscillatory relaxations. For Cu(110) a contraction of about 7.5% of the first interlayer spacing d_{12} and an expansion of about 2.5% of the second interlayer spacing d_{23} have been measured[21]. Baddorf *et al.*[20] observed that both lattice spacings return linearly to the bulk spacing with hydrogen coverage. The H atoms appear to eliminate the charge redistribution which originally caused the relaxation. The same authors have also monitored, by means of specular

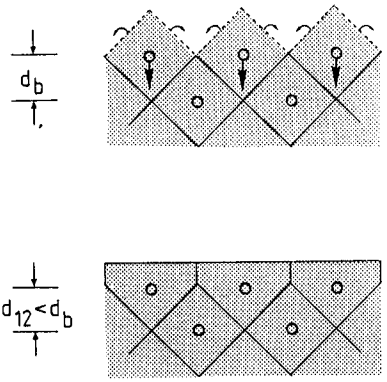

Fig. 7. Surface relaxation in the charge smoothing model of Smoluchowski[17].

EELS, the frequency of the A_1-phonon at the $\bar{\Gamma}$-point (see section 3.3) upon hydrogen adsorption. A decrease in phonon energy has been observed, which could be related to the increasing lattice spacing d_{12} through $\hbar\omega \sim d_{12}^{1.8\pm0.7}$. In the framework of a simple central force constant model, including only nearest neighbor interactions, this dependency can be use to link surface force constants with the interlayer spacing of Cu(110). Baddorf and Plummer[22] obtained:

$$\Phi''_{12}/\Phi''_b \sim (d_b/d_{12})^{7.3\pm3} \tag{15}$$

3.2. He atoms and surface phonons

He atoms, which are scattered at a surface, are characterized by their incoming and outgoing wavevectors $\vec{k}_i$ and $\vec{k}_f$ and energies $E_i = \hbar k_i^2/2m$ and $E_f = \hbar k_f^2/2m$, with m being the mass of the He atom. If we denote the incident and outgoing angle with respect to the surface normal by ϑ_i and ϑ_f, the projected wavevectors parallel to the surface are given by $\vec{K}_i = \vec{k}_i \sin\vartheta_i$ and $\vec{K}_f = \vec{k}_f \sin\vartheta_f$. The kinematic conditions for scattering are derived from energy and momentum conservation. Because of the loss of vertical translational invariance at the surface, only the momentum parallel to the surface is

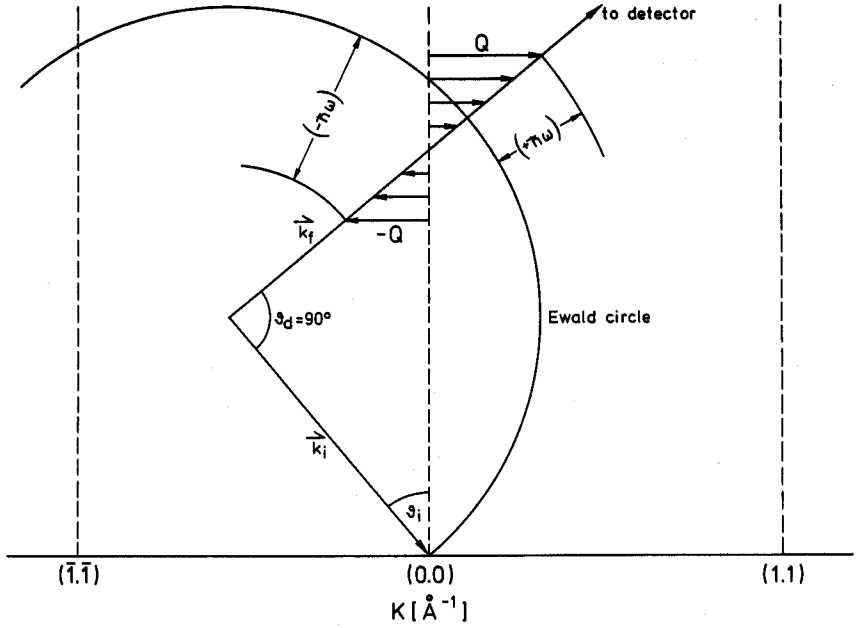

Fig. 8. Ewald diagram of inelastic He scattering from a clean metal surface, for $\vec{G} = 0$.

conserved in the scattering process:

$$E_i = E_f - \hbar\omega(\vec{Q}_\parallel) \tag{16}$$

$$\vec{K}_i = \vec{K}_f - (\vec{Q}_\parallel + \vec{G}) = \vec{K}_f + \Delta\vec{K} \tag{17}$$

with $\hbar\omega$ being the phonon energy, $\vec{Q}_\parallel$ the wavevector of the phonon parallel to the surface and $\vec{G}$ a reciprocal lattice vector of the crystal surface. According to the sign of ω a phonon is annihilated ($\omega > 0$) or created ($\omega < 0$) during the scattering process. In Fig. 8 the inelastic scattering process is described in terms of an Ewald diagram. For planar scattering with fixed scattering angle $\vartheta_d = \vartheta_i + \vartheta_f = 90°$, the combination of energy and momentum conservation leads to the following relation between ω and ΔK, known as a 'scan curve':

$$\omega = \frac{\hbar k_i^2}{2m}\left[\frac{\sin\vartheta_i + (\Delta K/k_i)}{\cos\vartheta_i}\right]^2 - \frac{\hbar k_i^2}{2m} \tag{18}$$

In Fig. 9 we show a family of scan curves, with the incident angle ϑ_i as parameter, for He atoms of incident energy 18 meV (thick lines). The

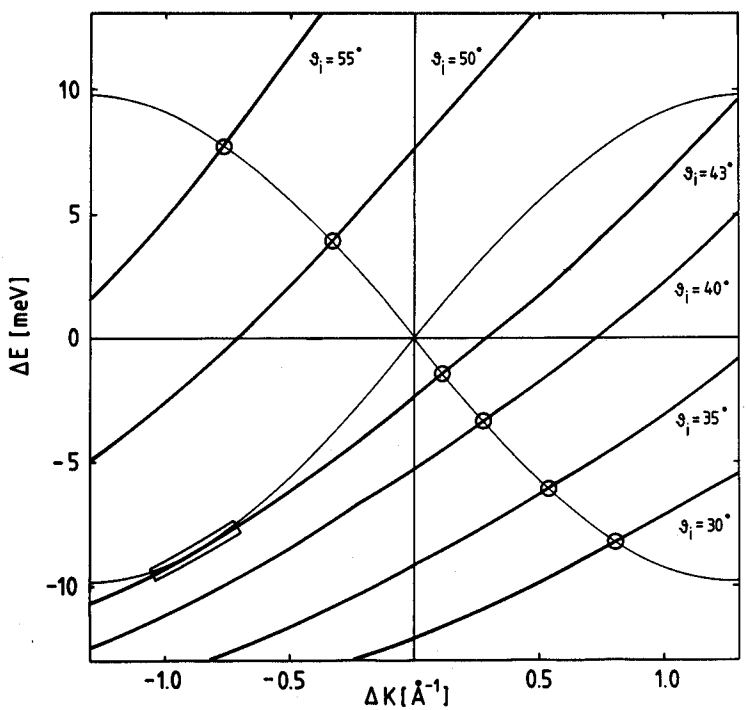

Fig. 9. Kinematics of surface phonon He spectroscopy. The thick lines correspond to scan curves of a 18 meV He beam. The thin lines display the Rayleigh phonon dispersion curve of Pt(111) along the $\bar{\Gamma}$ $\bar{M}$ azimuth.

theoretical dispersion curve of the Pt(111) Rayleigh wave along the $\bar{\Gamma}\bar{M}$ azimuth is also plotted (thin lines). Phonon excitation can only occur when the scan and dispersion curves intersect. Figure 9 illustrates in a very simple way the experimental procedure to obtain dispersion curves: TOF spectra are measured for various incident angles at a fixed incident beam energy.

The fulfillment of the kinematical relation is only a necessary but not a sufficient condition for detecting a particular surface phonon in an inelastic He scattering experiment; the dynamical scattering cross-section for this process has to be large enough. Manson and Celli have calculated the dynamical reflection coefficients for He scattering in the distorted wave Born approximation[23]. This approximation is valid as long as single phonon scattering only is considered. Weare[24] gives an estimate of the importance of multiphonon events. For surface temperatures

$$T_s < \frac{m_s}{m_{He}} \frac{k_B \theta_s^2}{100 E_{iz}} \tag{19}$$

he estimates one-phonon processes to be dominant. Here, E_{iz} is the energy component of the He atom normal to the surface, m_s the mass of the surface atoms and θ_s the surface Debye temperature. The latter has been determined for Pt(111) in He scattering experiments to be $\theta_s = 231$ K. In this limit Manson and Celli deduced for a one-phonon inelastic process the following differential reflection coefficient:

$$\frac{d^2R}{dE_f\, d\Omega_f} \sim \sum_{\vec{Q},j} |\vec{e}(\vec{Q},j) \langle \psi_G^{f*} | \nabla U(\vec{Q},z) | \psi_G^i \rangle|^2 |n^{\pm}| \delta(\vec{K}_f - \vec{K}_i - \vec{Q}) \times \delta(E_f - E_i - \hbar\omega(\vec{Q},j)) \tag{20}$$

This formula describes the exchange of a single phonon of wavevector $\vec{Q}$, frequency $\omega(\vec{Q},j)$ and polarization $\vec{e}(\vec{Q},j)$. $n^{\pm}$ is the Bose factor for annihilation $(-)$ or creation $(+)$ of a phonon, respectively, i.e. the phonon occupation number.

Equation (20) contains the matrix elements between the initial and final states of the $(\vec{Q} - \vec{G})$ component of the He surface potential gradient ∇U. The potential gradient can be thought of as vector with normal component $dU_{\vec{Q}-\vec{G}}/dz$ and parallel component $i(\vec{Q} - \vec{G})\, U_{\vec{Q}-\vec{G}}$. Because in general $dU_{\vec{Q}-\vec{G}}/dz > |i(\vec{Q} - \vec{G})\, U_{\vec{Q}-\vec{G}}|$, the major contribution to the scattering cross-section for inelastic one-phonon events is due to the phonon modes with polarizations normal to the surface.

The first successful measurement of surface phonons by means of inelastic He scattering was performed in Göttingen in 1980[25]. By using a highly monochromatic He beam ($\Delta v/v \approx 1\%$) Brusdeylins *et al.* were able to measure the dispersion of the Rayleigh wave of the LiF(001) crystal surfae. In earlier attempts[26,27] the inelastic events could not be resolved satisfactorily due to the low beam monochromaticity. In Fig. 10a we show a typical TOF spectrum,

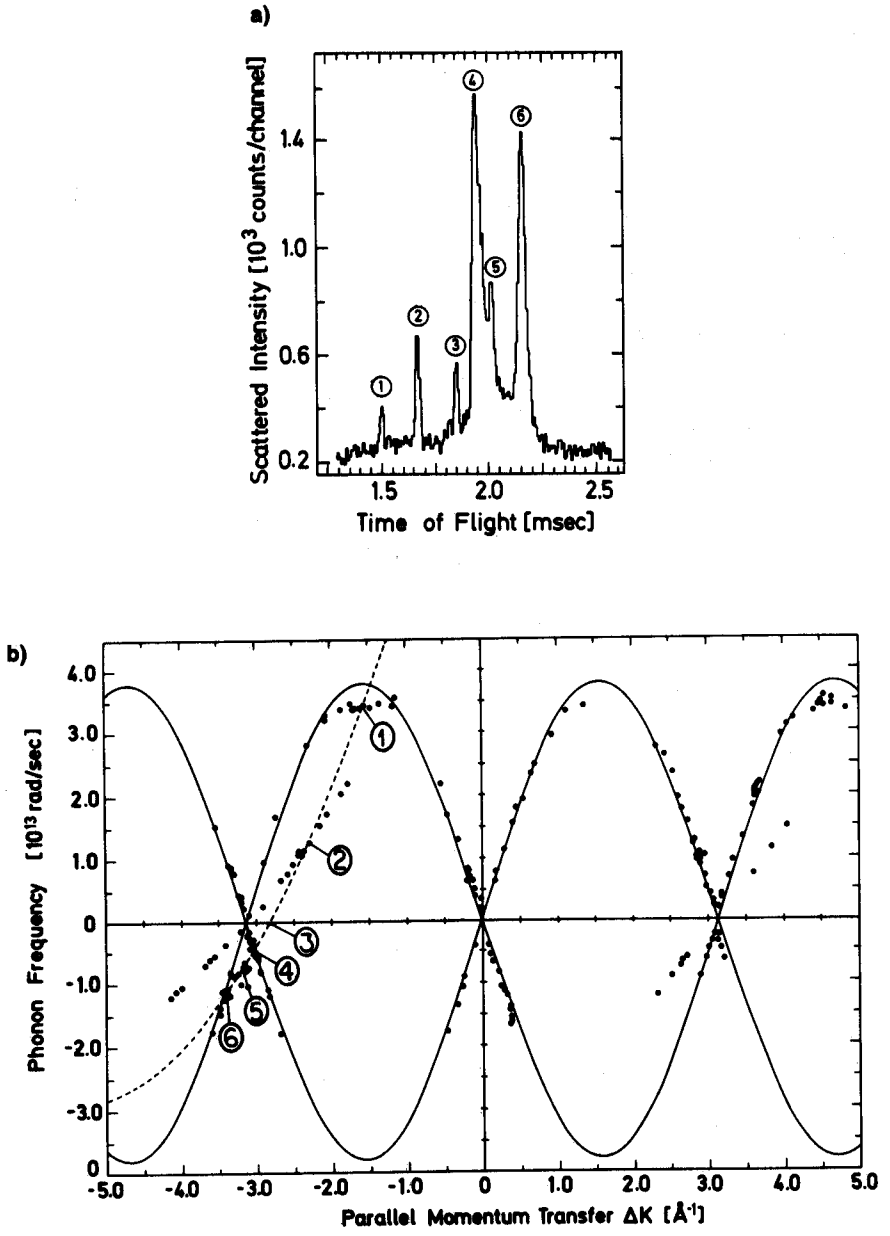

Fig. 10. (a) He time-of-flight spectrum taken from a LiF(001) surface along the ⟨100⟩ azimuth at an incident angle $\vartheta_i = 64.2°$. The primary beam energy was 19.2 meV. (*After Ref. 25.*). (b) Measured Rayleigh phonon dispersion curve of LiF(001) ⟨100⟩, including a scan curve (dashed) for the kinematical conditions in (a). (*After Ref. 25.*)

measured from a LiF(001) crystal at an incident angle $\vartheta_i = 64.2°$. Two energy gain peaks (1 and 2) and three energy loss peaks (4–6) are clearly resolved. They are associated with phonon annihilation and phonon creation, respectively. The peak 3 is elastic. From the comparison with the scan curve (dashed) and the Rayleigh dispersion curve (solid) of LiF in Fig. 10b, peaks 1, 4 and 6 are associated with Rayleigh phonons. Peak 5 has been attributed by the authors to a bulk phonon. Peak 2 is an instrumental artifact. It is due to the elastic diffraction of the very low intensity, but broad velocity distribution wings of the He nozzle beam. These 'ghost' peaks have been named 'deceptons'.

Since the initial experiment with alkali halides of the Göttingen group, the surface phonon dispersion of numerous other materials including metal and semiconductor surfaces as well as adsorbate systems has been measured by inelastic He scattering. As any other method, the use of He scattering as surface vibrational spectroscopy has also its limits. The first has been emphasized above in connection with the single-phonon reflection coefficient evaluated by Manson and Celli: He atoms mainly probe vibrations with perpendicular polarization. The second limit originates in the nature of the gas surface scattering interaction itself. Thermal He atoms are scattered by the repulsive part of the surface potential at appreciable distances above the surface (~ 3–4 Å). At these distances the phonon-induced corrugation in the charge density is attenuated, because – depending on the lateral position – it may reflect the

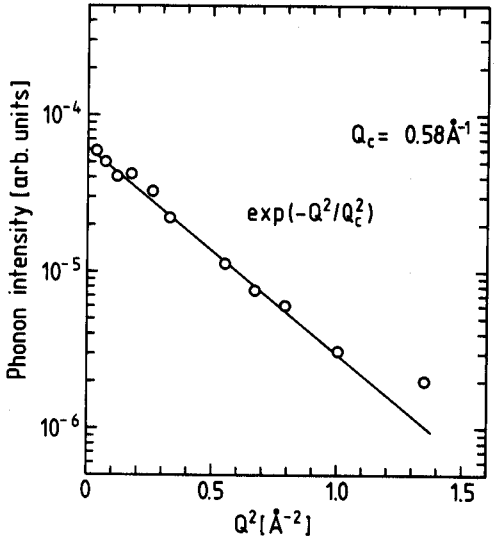

Fig. 11. Measured decrease of inelastic scattered He intensity (Rayleigh wave) from Pt(111) with increasing momentum transfer.

vibration of more than one surface atom. Taking into account, in addition, that the incoming He atom has a size comparable to the lattice spacing, its interaction with the charge density can be viewed as a collision with more than one surface atom. As a result, surface vibrations may be averaged out. The effect is usually cited as the 'Armand effect'[28]. Obviously, the effect dominates at the zone boundary, where neighboring atoms are vibrating in antiphase.

In Fig. 11 we have plotted the intensity of the inelastic Rayleigh phonon peak in He energy loss spectra taken from a Pt(111) surface along the $\bar{\Gamma}\bar{M}$ azimuth. The intensities have been extracted from TOF spectra taken with a primary He beam energy of 27 meV at a surface temperature of 105 K. All data have been corrected for the Bose factor and plotted on a semilogarithmic scale as a function of the square of the momentum transfer. The intensity rapidly decreases with increasing wavevector. The data quantitatively follow a Gaussian fall-off [$\sim \exp(-Q^2/Q_c^2)$], with a cut-off wavevector $Q_c = 0.58\ \text{Å}^{-1}$. Such a Gaussian fall-off of the Rayleigh phonon intensity has been predicted

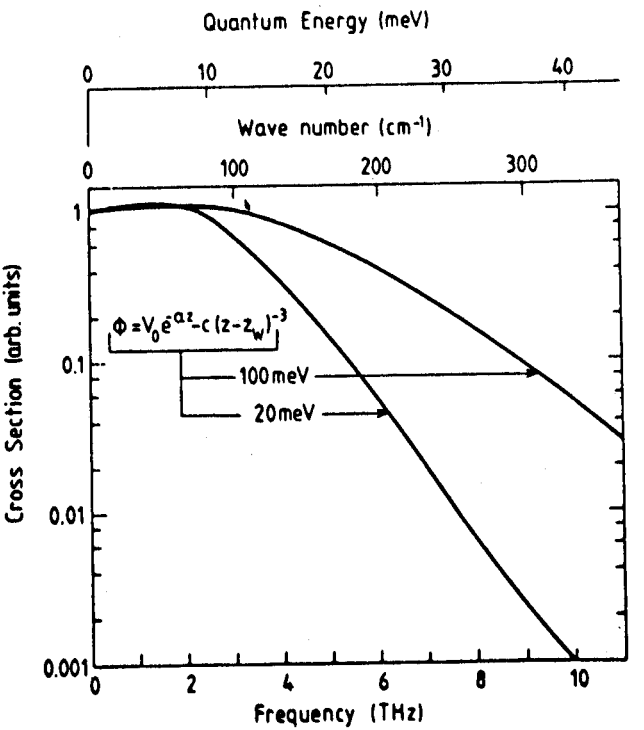

Fig. 12. Inelastic one-phonon He scattering cross-section (He beam energy 20 meV and 100 meV) as a function of phonon frequency. (*After Ibach*[32].)

by Bortolani *et al.*[29] in the framework of the distorted wave Born approximation. For Ag(111) they have calculated a cut-off value $Q_c = 0.74\,\text{A}^{-1}$.

In addition to the Armand correction, the substrate vibrations can be averaged out due to the finite interaction time between the He atom and the surface (the 'Levi effect'[30]). This is the reason why it is impossible to map out complete dispersion curves with inelastic scattering of the even slower Ne atoms[31]. This effect is also important for He scattering, especially when looking for high frequency modes. Ibach[32] has quantified this 'slow collision efect' by evaluating the single-phonon cross-section for He scattering from Cu(110), using the Harris–Liebsch[33] potential, as a function of phonon frequency. Ibach's results for 20 meV and 100 meV beams are shown in Fig. 12. The strong decrease of the cross-section with increasing phonon frequency is obvious. The effect can be partially counterbalanced by using higher beam energies. According to Eq. (19), however, the multiphonon background increases strongly with the beam energy; thus this alternative appears not that desirable.

The highest phonon frequency measured so far has been reported for NaF(100). By using primary beam energies of 90 meV, Brusdeylins *et al.*[34] have detected optical surface modes with frequencies of ~ 40 meV. The intensities, however, were rather low and the multiphonon background dominated the energy loss spectra.

In the following sections, some systems which have been investigated by means of inelastic He scattering are discussed in some more detail.

3.3. Surface dynamics of Cu(110)

Recently, we have measured the surface phonon dispersion of Cu(110) along the $\bar{\Gamma}\bar{X}$, $\bar{\Gamma}\bar{Y}$, and $\bar{\Gamma}\bar{S}$ azimuth of the surface Brillouin zone (Fig. 13) and analyzed the data with a lattice dynamical slab calculation[35]. As an example we will discuss here the results along the $\bar{\Gamma}\bar{X}$-direction, i.e. the direction along the close-packed Cu atom rows.

In Fig. 14 two characteristic TOF spectra taken along the $\bar{\Gamma}\bar{X}$ azimuth are

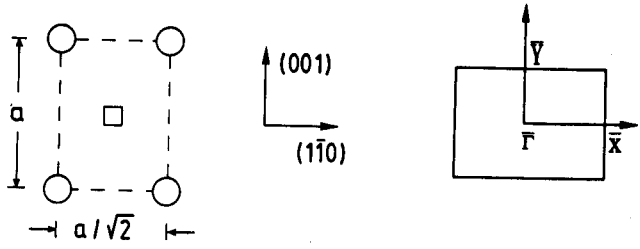

Fig. 13. Real and reciprocal lattice of the Cu(110) surface.

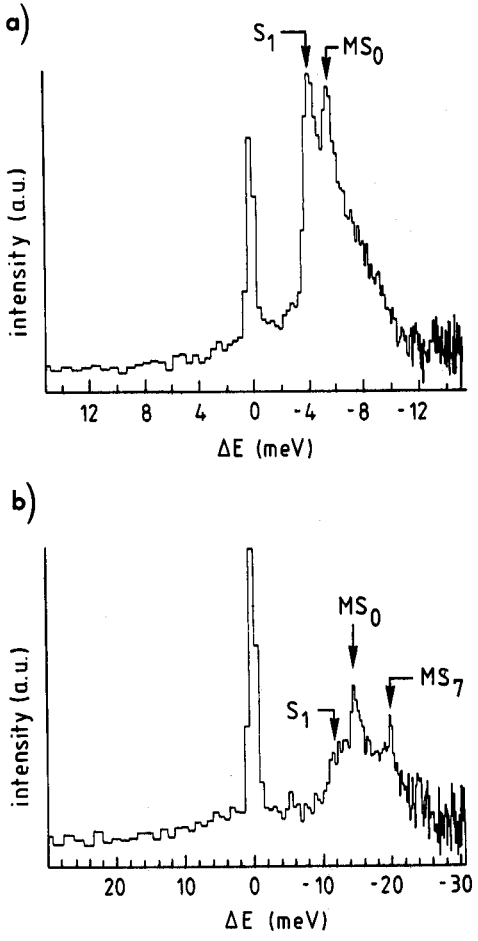

Fig. 14. He energy loss spectra taken from Cu(110) along the $\bar{\Gamma}\,\bar{X}$ azimuth at $\vartheta_i = 38°$ (a) and 35° (b), respectively. The primary He beam energy was 39.6 meV.

shown. The primary He beam energy was 39.6 meV and the angles of incidence 38° and 35°, respectively. The Rayleigh phonon S_1 and two other surface phonon losses, indicated by MS_0 and MS_7 are detected. In Fig. 15 the surface phonon dispersions are plotted, as obtained from numerous TOF spectra like those in Fig. 14 taken at different beam energies and incident angles. According to the early analysis of Allen *et al.*[12], the lowest energy phonon branch is the Rayleigh wave (S_1). The Rayleigh phonon loss S_1 is the dominant feature in the energy loss spectra for small energy transfers. Upon sampling

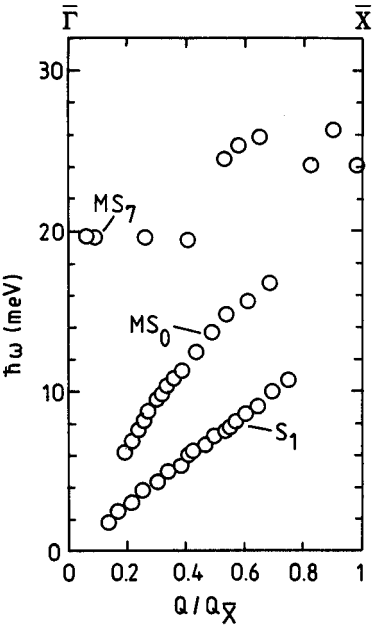

Fig. 15. Measured surface phonon dispersion of Cu(110) along the $\bar{\Gamma}$ $\bar{X}$ azimuth.

larger energy transfers the intensity of the energy loss assigned by MS_0 increases relative to the Rayleigh phonon S_1. However, approaching the zone boundary, the intensity of both phonon losses drops dramatically; in the last quarter of the zone both disappear in the background. At small wavevectors the phonon losses MS_0 are located close to the shear horizontal mode S_2 predicted by Allen *et al.*[12]. However, because selection rules exclude the coupling of He atoms to odd modes, the MS_0 energy losses observed correspond to a resonance not predicted by Allen *et al.*[12].

In addition to the acoustical modes S_1 and MS_0, we observe in the first half of the Brillouin zone a weak optical mode MS_7 at 19–20 meV. This particular mode has also been observed by Stroscio *et al.*[36] with electron energy loss spectrocopy. According to Persson *et al.*[37] the surface phonon density of states along the $\bar{\Gamma}\bar{X}$-direction is a region of depleted density of states, which they call pseudo band-gap, inside which the resonance mode MS_7 peals of. This behavior is explained in Fig. 16: (a) top view of a (110) surface; (b) and (c) schematic plot of the structure of the layers in a plane normal to the (110) surface and containing the (110) and (100) directions, respectively. Along the (110) direction each bulk atom has six nearest neighbors in a lattice plane, while in the (100) direction it has only four. As exemplified in Fig. 17, where inelastic

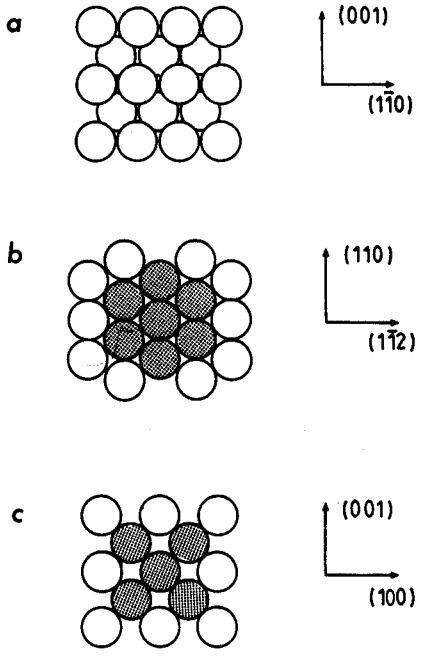

Fig. 16. Structure of f.c.c crystals; (a) top view of a Cu(110)-surface; (b) and (c) view of bulk planes normal to the (110)-surface plane and containing the (110) and (100) directions, respectively.

neutron scattering data for bulk Cu along the (110) and (100) directions are shown, this causes the restoring force along the (110) direction to be stronger (and thus the frequency to be larger) in the middle of the Brillouin zone than at the zone boundary, whereas in the (100) direction the frequency increases monotonically. Due to the non-monotonic behavior of the dispersion curve along the (110) direction, the projected phonons on a bulk plane have a large density of states in the range 21 meV $\lesssim \hbar\omega \lesssim$ 26.5 meV and a very low density below 21 meV (see Fig. 18, upper part). This allows a localized mode to peal off at the surface (surface density of states shown in the lower part of Fig. 18). Due to the low, but still not vanishing density of states, this mode turns to be a surface resonance.

The frequency of the MS_7 mode is well suited to give some fix points for the lattice dynamical calculation. This is obvious by inspection of Fig. 19 which shows the displacement pattern of this mode at the $\bar{\Gamma}$ point (at $\bar{\Gamma}$ the MS_7 phonon corresponds to the A_1 symmetry group). The motions of the atoms being shear vertical, the lattice layers remain rigid planes; i.e. the frequency of

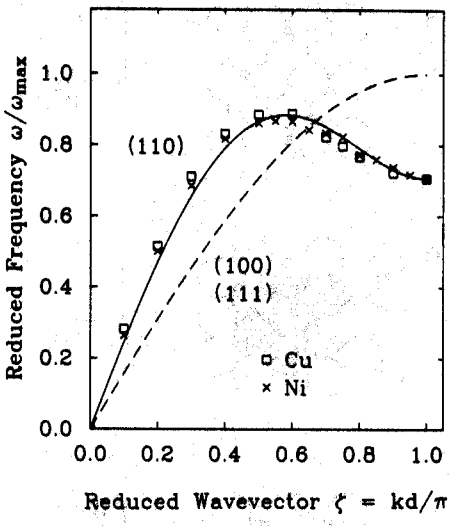

Fig. 17. Bulk phonon dispersion of longitudinal modes in Cu and Ni crystals, along the (110) and (100) directions. (*After Ref. 37.*)

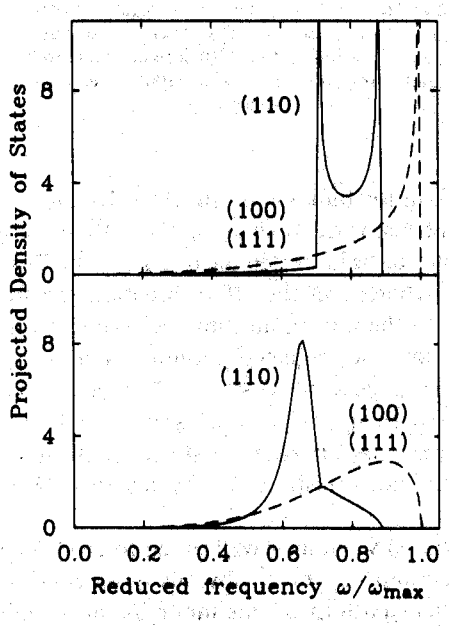

Fig. 18. Longitudinal bulk phonon density of states projected on bulk (top) and surface layers (bottom). (*After Ref. 36.*)

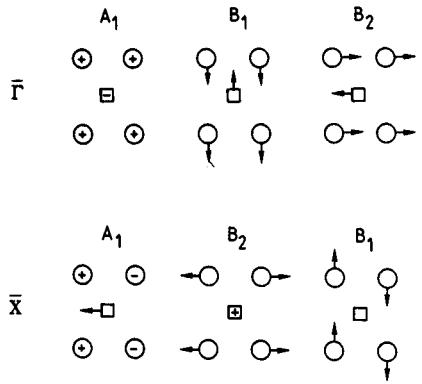

Fig. 19. Displacement patterns of the Cu(110) surface eigenmodes at $\bar{\Gamma}$ and $\bar{X}$.

the mode, in a simple nearest-neighbor central force model, is only affected by the interlayer force constant. Thus, we can determine the coefficient α in Badger's rule (Eq. (14)) by fitting the MS_7 frequency[38].

Before doing so, let us say a few words to the lattice dynamical model we have used to analyze the data. The lattice dynamics of the Cu atoms are treated in the harmonic approximation using pair potentials. The bulk phonon dispersion curves of Cu are well described by a single nearest-neighbor force constant model[39]. The potential energy term in the model Hamiltonian is based on nearest-neighbor interactions and central forces. Equilibrium conditions then require that the first derivative of the pair potential vanishes, i.e. each atom has it equilibrium position at the minimum of the pair potential connecting the atom to its next neighbor. However, in section 3.1 we have seen that upon creation of a surface, the electron charge density between the first few surface layers and also in between the atoms of a particular layer is rearranged. This charge rearrangement leads to the already noted interlayer relaxation, but also to an intralayer surface stress by modifying the pair potential in that its first derivative Φ'_{ij} becomes nonzero at equilibrium. The surface relaxation is actually the response to the interlayer stress; a relaxation of the atom positions in the surface plane which would be induced by the intralayer stress would be in fact a reconstruction. It is also obvious that surface stress affects the frequency of phonon modes with polarizations perpendicular to the stress (in order to increase the pitch of a violin string we have to tighten it). Lehwald *et al.*[38] were the first to account for this lateral surface stress in a lattice dynamical study of Ni(110). In this model, the stress along the high symmetry directions is given by the stress tensors:

$$\tau_{\bar{\Gamma}\bar{X}} = \Phi'_{11x}/a \tag{21}$$

$$\tau_{\bar{\Gamma}\bar{Y}} = \Phi'_{11y}\sqrt{2}/a \tag{22}$$

TABLE 2
Intralayer force constants of Cu(110) from scaling of the force constants according to Badger's rule with $\alpha = 8$ ($\Delta d_{12} = -7.5\%$, $\Delta d_{23} = +2.5\%$).

$\Phi^{\parallel}_{12}/\Phi^{\parallel}_{b}$	$\Phi^{\parallel}_{13}/\Phi^{\parallel}_{b}$	$\Phi^{\parallel}_{23}/\Phi^{\parallel}_{b}$	$\Phi^{\parallel}_{24}/\Phi^{\parallel}_{24}/\Phi^{\parallel}_{b}$
1.158	1.225	0.951	0.905

with a being the lattice constant (Fig. 13), Φ'_{11x} and Φ'_{11y} the first derivatives of the pair potential between nearest neighbors along the $\bar{\Gamma}\bar{X}$ and $\bar{\Gamma}\bar{Y}$ directions, respectively.

Let us now come back to Badger's rule. The parameter α is expected to lie somewhere between 5 and 10. By fitting the experimental MS_7 frequency of $\hbar\omega = 19.4$ meV with the lattice dynamical model described above, we find

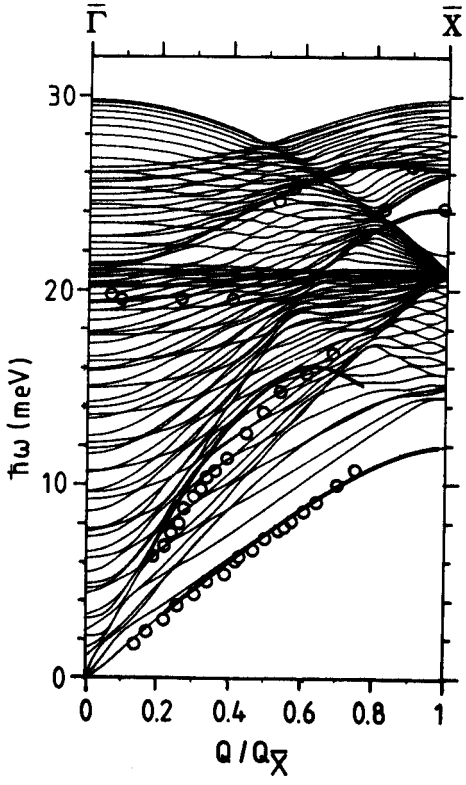

Fig. 20. Surface phonon dispersion curves of Cu(110) along the $\bar{\Gamma}\,\bar{X}$ azimuth calculated for a 30-layer slab with $\alpha = 8$; the data points are from Fig. 15.

a best-fit exponent $\alpha = 8$. This value is in good agreement with the relaxation analysis of Baddorf *et al.*[20,22] (Eq. (15)). In Table 2 we summarize the various force constants obtained with this value of the exponent α: The bulk force constant $\Phi_b'' = 2.73 \times 20^4$ dyn/cm is matched to the maximum bulk frequency $\hbar\omega_b = 29.7$ meV.

In Fig. 20 we show a theoretical dispersion plot using these parameters and a tensile stress $\tau_{\bar{\Gamma}\bar{X}} = 2.7 \times 10^3$ dyn/cm. Due to the symmetry of the modes at $\bar{X}$ the stress tensor $\tau_{\bar{\Gamma}\bar{Y}}$ does not affect the surface eigenmodes at this symmetry point. In addition, we have softened the intralayer force constant Φ_{11}'' in the first layer by about 10%. With these parameters, we find good agreement between experimental data and theoretical dispersion curves.

As already noted, the lowest mode S_1 is the Rayleigh wave. Throughout the Brillouin zone this mode exhibits significant vertical polarization. The resonance MS_0 along the edge of the longitudinal acoustic bulk modes has a large parallel component in the first third of the Brillouin zone. With increasing wavevector the vertical component increases and becomes dominant in the middle of the Brilliuin zone. In the last third, polarization changes again and at the $\bar{X}$ point the mode is a pure longitudinal mode. This is the reason why the MS_7 mode is observed in experiment only in the first part of the Brillouin zone. The MS_7 resonance is nearly dispersionless and mainly vertically polarized. At reduced wavevectors 0.5–0.6 the resonance interacts with the MS_0 resonance producing an 'avoided crossing' with an interchange of character. In the bulk gap near the $\bar{X}$ point the resonance develops in a well-defined surface mode S_7 which is mainly longitudinally polarized.

3.4. Au(111), the influence of reconstruction on surface phonon dispersion

The (111) surfaces of the noble metals Cu, Ag, Au and Pt were the first metal surfaces to be studied systematically by means of inelastic He scattering[40–44]. Figures 21 and 22 show a series of He energy transfer spectra taken from Cu(111) and Au(111) along the $\bar{\Gamma}\bar{M}$ azimuth[41]. In the case of Cu(111) in all spectra at least two energy losses are resolved. The surface phonon dispersion curves obtained from numerous energy loss spectra, are shown in Fig. 23 for the (111) surface of Cu, Ag and Au by the black dots. The theoretical dispersion curves, also shown, have been calculated by Jayanthi *et al.* using a new approach[45] and will be discussed below. The low energy branch is the surface Rayleigh wave (S_1). The high energy phonon branch is located within the projected bulk phonon band. This feature is not consistent with a lattice dynamical model assuming a simple geometrical termination of the bulk crystal[12]. The feature is much too soft to be ascribed to the longitudinally polarized acoustical mixed mode[40]. Note that the same discrepancy is observed for the Ag and Pt(111) surface along this azimuth. All three surfaces (Cu, Ag, Pt) exhibit a similar anomalously soft acoustic phonon branch along the $\bar{\Gamma}\bar{M}$-azimuth.

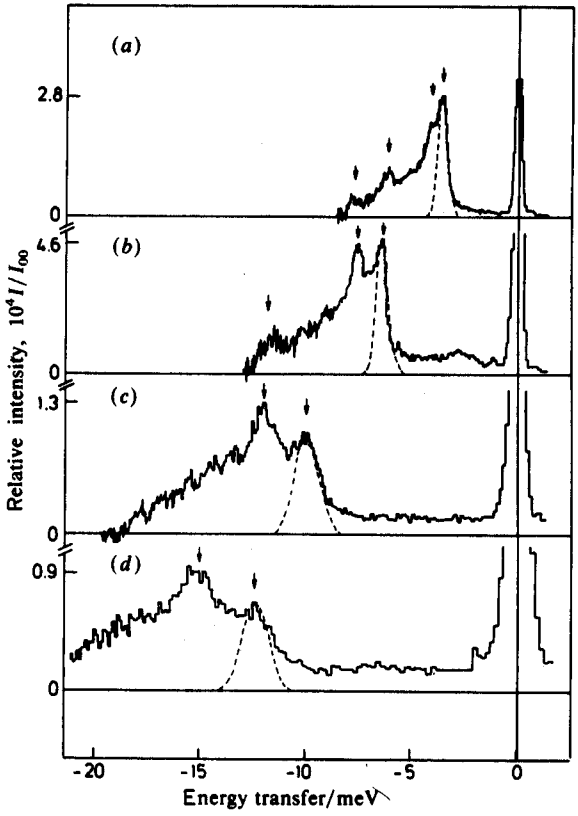

Fig. 21. He energy loss spectra taken from Cu(111) along the $\bar{\Gamma}\bar{M}$ azimuth. (a) $E_i = 12.7$ meV, $\vartheta_i = 38°$, (b) $E_i = 18.2$ meV, $\vartheta_i = 35°$, (c) $E_i = 31.5$ meV, $\vartheta_i = 35°$, (d) $E_i = 41.4$ meV, $\vartheta_i = 35°$. (*After Ref. 41.*)

It has been shown[46] that in the framework of a phenomenological force-constant model, it is possible to generate the anomalous phonon branch by assuming a substantial reduction of the in-plane surface force constant with respect to the bulk value. This force constant reduction causes a significant frequency decrease of the longitudinal phonon modes at the zone boundary. Bortolani *et al.*[46] have attributed this force constant reduction to the spilling of charge outside the surface and the resulting modification of the screening of the surface atoms. The force constant reduction necessary to fit the data amounted to about 50% (Cu, Ag) and 60% (Pt).

In the case of Au(111), the He energy loss spectra exhibit significantly broader inelastic peaks. Only in a few cases the existence of two components can be inferred. This behavior is only partly due to the lower Debye

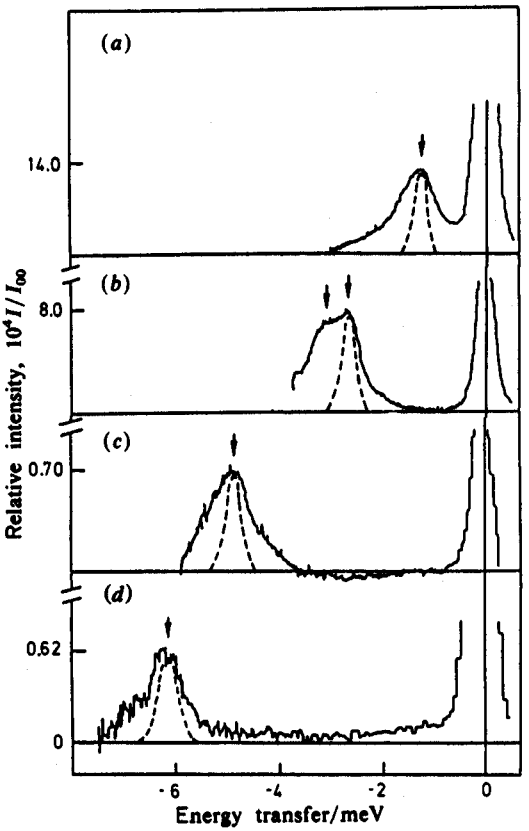

Fig. 22. He energy loss spectra taken from Au(111) along the $\bar{\Gamma}\ \bar{M}$ azimuth. (a) $E_i = 12.2$ meV, $\vartheta_i = 41°$, (b) $E_i = 12.2$ meV, $\vartheta_i = 36°$, (c) $E_i = 12.2$ meV, $\vartheta_i = 28°$, (d) $E_i = 14.6$ meV, $\vartheta_i = 24°$. (*After Ref. 41.*)

temperature (multiphonons). As will be shown in section 4.2.3, the clean Au(111)-surface is reconstructed with a $(23 \times \sqrt{3})$ unit cell. This reconstruction has a marked influence on the surface phonon displacement field, which becomes obvious by inspection of Fig. 23. Two extremely soft acoustic phonon branches, one of which is the Rayleigh wave, exist below the transverse bulk band edge. No acoustic resonance mode within the projected bulk bands is observed.

The model of Jayanthi *et al.*[45] overcomes the phenomenological force-constant models and thus avoids the large number of hypothetical force constants, sometimes used in these calculations. Jayanthi *et al.* calculate the charge density in each unit cell by an expansion over many-body interactions, which arise from the coupling of the electronic deformations to

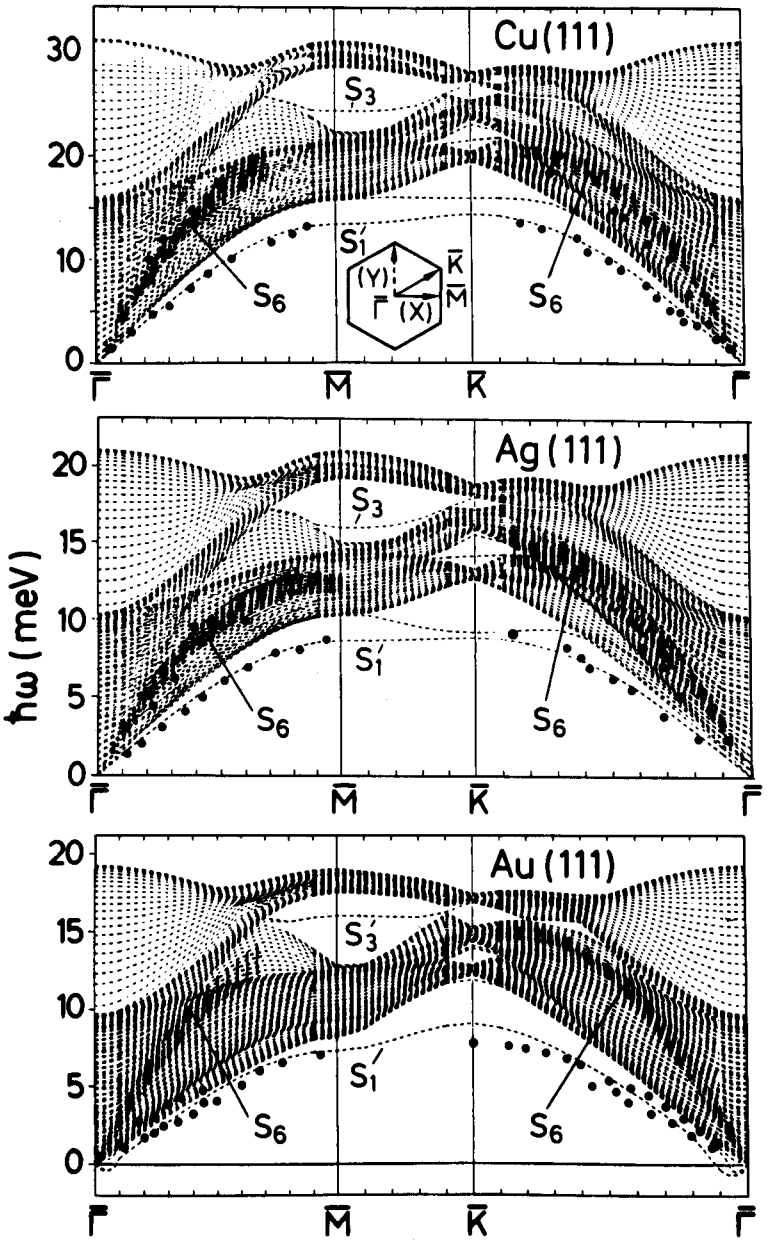

Fig. 23. Calculated[45] and measured[41] surface phonon dispersion curves of the (111) surfaces of the noble metals Cu, Ag and Au. (*After Ref. 45.*)

the displacement field. This model is appealing because of the small number of parameters and because all parameters have a direct microscopic meaning and may be obtained from *ab initio* calculations.

The calculated Rayleigh mode (S_1), the lowest lying phonon branch, is in good agreement with the experimental data of Harten *et al.*[41] for all three metals. Due to symmetry selection rules the shear horizontal mode just below the transverse bulk band edge can not be observed by scattering methods. The mode denoted by S_6 is the anomalous acoustic phonon branch discussed above. Jayanthi *et al.* ascribed this anomalous soft resonance to an increased Coulomb attraction at the surface, reducing the effective ion–ion repulsion of surface atoms. The Coulomb attraction term is similar for all three metals ($\sim -4 \times 10^4$ erg/cm^2); the repulsive forces are, however, larger in Au than in Cu and Ag (~ 3.5 and $\sim 2.5 \times 10^4$ erg/cm^2, respectively), preventing the development of a *soft* S_6 resonance on the Au(111) surface. In addition, Jayanthi *et al.* deduced for the Au(111) soft surface phonons with imaginary frequencies (in the first tenth of the Brillouin zone), indicative for surface reconstruction (see section 4.2.3). The S_3 mode in the band gaps were not detected by Harten *et al.*[41] for the metals Cu, Ag, Au, but have been detected by Kern *et al.*[43] for Pt.

3.5. Dynamical coupling between adsorbate and substrate

Despite the high energy resolution and extreme surface sensitivity only few studies on the dynamics of adsorbate covered surfaces have been performed so far by He scattering[47–51]. However, the vibrational states of adsorbates are relevant for most dynamical surface processes like scattering, accommodation, desorption, or diffusion, and therefore, their nature and relaxation dynamics deserve more attention.

In chemisorbed systems, the molecular orbitals of the adsorbate are mixed with the electronic states of the substrate, producing strong adsorption bonds, i.e. the frequency of the adsorbate mode is well above the highest phonon frequency of the substrate. The relaxation of these vibrational excited states via emission of substrate phonons has only a low probability, because many phonons have to be emitted during the decay. Non-radiative damping by electron–hole pair excitation appears to be the dominant relaxation path in these systems.

In physisorbed systems, the electronic ground state of the adsorbate is only weakly perturbed upon adsorption. The physisorption potential is rather flat and shallow, i.e. the restoring force of the vertical motion of adatoms is weak, and thus, the corresponding adsorbate–substrate vibrations are low-frequency modes[50,51]. Radiative phonon processes are expected to dominate the relaxation and coupling processes.

Hall, Mills and Black[52] have explored the phonon-mediated coupling

between physisorbed rare gas atoms and Ag substrate atoms in the framework of a simple lattice dynamical model. The observed coupling effects can best be illustrated with the normal mode spectrum of a physisorption system, shown in Fig. 24. At the zone boundary of the Brillouin zone the adlayer mode which is assumed to be dispersionless in accordance with experimental observations lies well below the substrate modes. Approaching the zone center, the adlayer mode inevitably intersects the substrate Rayleigh wave and finally, close to the zone center, the adlayer mode and the projected substrate bulk bands overlap. The results of the calculations show that near the zone boundary $\bar{M}$ (the $\bar{\Gamma}\bar{M}$ direction has been explored), where the substrate phonon frequencies are well above those of the adlayer, the influence of the substrate–adlayer coupling is small.

The predicted anomalies introduced by the coupling near the zone center $\bar{\Gamma}$ are twofold:

1. A dramatic hybridization splitting around the crossing between the dispersionless adlayer mode and the substrate Rayleigh wave (and a less dramatic one around the crossing with the $\omega = c_l Q_\parallel$ line – due to the Van Hove singularity in the projected bulk phonon density of states).
2. A substantial linewidth broadening of the adlayer modes in the whole region near $\bar{\Gamma}$ where they overlap the bulk phonon bands of the substrate: the excited adlayer modes may decay by emitting phonons into the substrate; they become leaky modes. These anomalies were expected to extend up to trilayers even if more pronounced for bi- and in particular for monolayers.

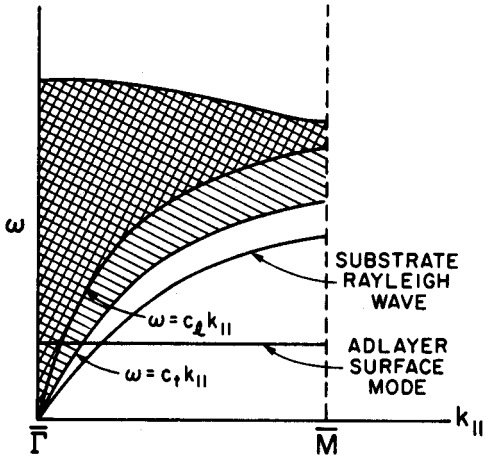

Fig. 24. Schematic normal mode spectrum of a rare gas monolayer physisorbed on a single crystal surface. (*After Ref. 52.*)

Experimental data of Gibson and Sibener[53] appears to confirm qualitatively these predictions at least for monolayers. The phonon linewidths were broadened around $\bar{\Gamma}$ up to half of the Brillouin zone. The hybridization splitting could not be resolved, but an increase of the inelastic transition probability centered around the crossing with the Rayleigh wave and extending up to 3/4 of the zone has been observed and attributed to a resonance between the adatom and substrate modes.

Recent measurements performed on Ar, Kr and Xe layers on Pt(111)[54] with a substantially higher energy resolution ($\Delta E \leqslant 0.4$ meV) have now confirmed quantitatively the theoretical predictions on the coupling effects within almost every detail (the hybridization around the van Hove singularity has only been seen in the case of Ar). The sequence of He TOF spectra in Fig. 25 taken along the $\bar{\Gamma}\bar{K}$-direction of a full Kr monolayer at 25 K gives a vivid picture of the coupling effects. The last spectrum $\vartheta_i = 37°$, taken near the zone boundary $\bar{M}$ exhibits a unique, sharp loss $\Delta E \approx -3.7$ meV resulting from the creation of an Einstein Kr monolayer phonon (perpendicular Kr–Pt vibration); its width corresponds to the instrumental width of $\Delta E \simeq 0.38$ meV, there is no linewidth broadening near the zone boundary. On the other hand, the Kr phonon peak in the first spectrum $\vartheta_i = 40°$ taken near the $\bar{\Gamma}$ point and located at $\Delta E \simeq -3.9$ meV is broadened by more than 0.5 meV. Of particular interest is also the small peak at $\Delta E \simeq -3.1$ meV, close to the position of the Pt substrate Rayleigh wave. The next two spectra, $\vartheta_i = 39.5°$ and 39°, taken always closer to the crossing between the Pt substrate Rayleigh wave and the Kr Einstein mode demonstrate strikingly the effect of the hybridization of the two modes: the originally tiny Pt peak increases dramatically, while the Kr peak is pushed slightly toward larger energies. After surpassing the crossover the higher energy loss disappears abruptly. As predicted[52], the two features in the doublet have comparable intensity only quite near the crossover.

Figure 26 shows the dispersion curve of the Kr monolayer obtained from a large number of spectra like those in Fig. 25. The hybridization splitting around the crossing with the substrate Rayleigh wave (solid line) is clearly observed. Also the predicted tiny frequency upshift close to the $\bar{\Gamma}$ point due to the coupling to the substrate vibrations is seen. The observed linewidth broadening is also shown in Fig. 26. As a measure of the broadening, the quantity $\Delta\varepsilon = [(\delta E)^2 - E_I^2]^{1/2}$, with δE the FWHM of the major loss feature and E_I the intrinsic instrumental broadening ($E_I = 0.38$ meV in the present experiment), is plotted as a function of the wavevector. A broadening larger than 0.5 meV is seen, and – as predicted – confined to the region near $\bar{\Gamma}$, where the adlayer mode overlaps the bulk bands of the substrate.

It is noteworthy that the phonon anomaly, due to the dynamical coupling between substrate Rayleigh wave and adlayer mode, is likewise present in the bi- and even the trilayer films[54]. It is only the Q range of the anomaly which

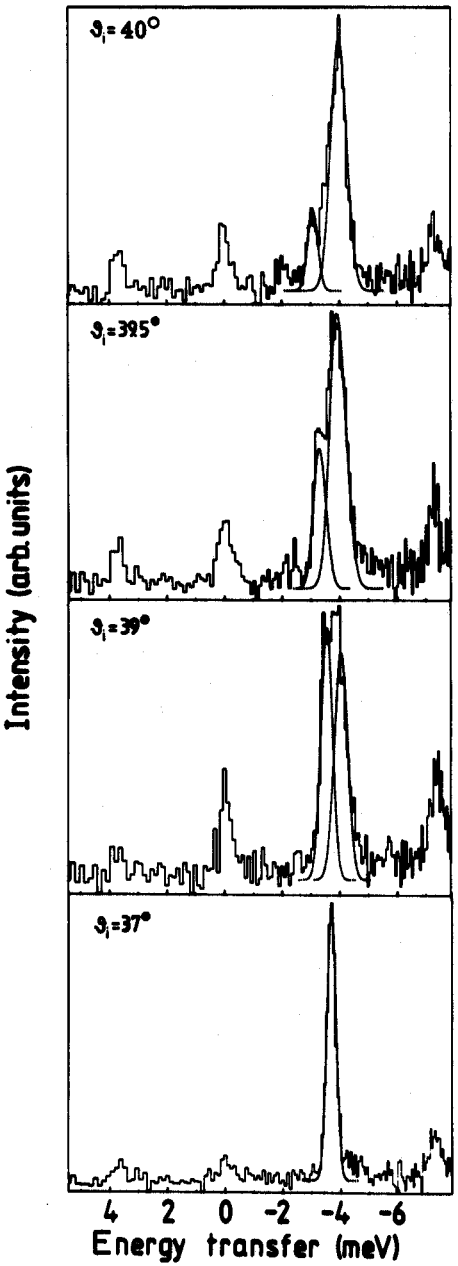

Fig. 25. He energy loss spectra from a Kr monolayer taken along the $\bar{\Gamma}\,\bar{K}_{Kr}$ azimuth. With decreasing incident angle ϑ_i, phonons with larger wavevectors are sampled.

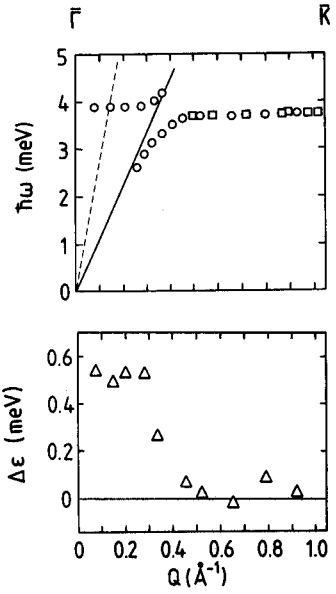

Fig. 26. Experimental dispersion curve of the Kr monolayer and measured line width broadening $\Delta\varepsilon$ of the Kr creation phonon peaks. The solid line in the dispersion plot is the clean Pt(111) Rayleigh phonon dispersion curve and the dashed line the longitudinal phonon bulk band edge of the Pt(111) substrate, both in the $\bar{\Gamma}\,\bar{M}_{Pt}$ azimuth which is coincident with the $\bar{\Gamma}\,\bar{K}_{Kr}$ azimuth.

becomes smaller, and its location shifts towards the zone center together with the location of the intersection between the Kr and the substrate Rayleigh mode. Linewidth broadening, due to radiative damping into the substrate bulk bands, has been found to be still substantial for bilayer films, while the trilayer shows no evidence for additional broadening.

4. SURFACE PHASE TRANSITIONS

4.1. Ordering in two dimensions

Solid surfaces of single crystals provide to some extent the realization of a well-defined two-dimensional (2D) periodic array of atoms. However, the loss of vertical translational invariance at the surface changes the local force field with respect to the bulk forces. As seen in section 3 the charge redistribution is

responsible for noticeable interlayer relaxations in the near surface region. In addition, the changes in the force field can also favor lateral atomic rearrangements in the surface plane. The surface 'reconstructs' into a phase with new symmetry. These reconstructive surface phase transitions can either occur spontaneously or be activated by temperature or by small amounts of adsorbates. Surface reconstruction has been observed on a number of metal and semiconductor surfaces (for a recent review, see Refs. 55 and 56). The most thoroughly studied reconstruction is apparently the (7×7) reconstruction of the Si(111) surface[57].

Even closer to the idea of 2D phases and their mutual transitions are adsorbed monolayers on single crystal surfaces. In analogy to bulk matter, these adsorbed layers can form quasi 2D gas, liquid or solid phases[58,59]. Of particular interest are the solid phases; the substrate provides a periodic potential relief which interferes with the lattice structure of the monolayer, inducing modulations in the latter. In addition, the adatoms being of a different kind than the substrate atoms, the strength of the lateral interactions within the adlayer differs in general from the strength of the adsorbate–substrate interaction. Depending on the delicate balance between these forces and on structural relationships, the adsorbed monolayer can form ordered solid structures which are commensurate (in registry) or incommensurate (out of registry) with the substrate.

4.1.1. Critical fluctuations and defects

In contrast to bulk phase transitions, phase transitions at surfaces are quite often high-order transitions. According to Ehrenfest, phase transitions are termed high order if the higher but not the first derivative of the free energy becomes discontinuous; i.e. high-order phase transitions exhibit a continuous change of state from one phase to the other, in contrast to first-order transitions, where a sudden rearrangement occurs.

Continuous transitions are characterized by a critical 'behavior' of a physical observable, which is the order parameter γ of the transition. Above the transition temperature T_c the thermodynamic average of the order parameter $\langle\gamma\rangle$ is zero, indicative of complete loss of long-range order. Below T_c the value of $\langle\gamma\rangle$ is nonzero indicating long-range order, and follows a power law when approaching the critical temperature:

$$\langle\gamma\rangle \sim (T_c - T)^{\beta} \tag{23}$$

The order parameter can be the magnetization in ferromagnetic materials, the electron pair amplitude in superconducting materials, the He^4 amplitudes in superfluid He^4 or the lattice distortion in crystals.

Such continuous phase transitions are conveniently described in a phenomenological Landau free-energy expansion of the order parameter. Since we

are dealing with two-dimensional lattices, two-component order parameters have to be choosen, which are parameterized by an amplitude and a phase. While phase fluctuations dominate the low-temperature behavior of two-dimensional phases, amplitude fluctuations dominate at higher temperatures when approaching the critical temperature. Indeed, phase fluctuations, in form of long-wavelength phonons, are responsible for the supression of a genuine long-range order in two-dimensional solid, at all temperatures $T > 0\,\mathrm{K}$. Amplitude fluctuations, which are always present and dominate at the phase transitions at high enough temperatures, appear in two-dimensional systems in the form of defects, in particular as dislocations in two-dimensional solids. Such dislocations (often termed domain walls or solitons) result by adding or removing a half-infinite row of atoms from an otherwise perfect lattice. They play a central role in phase transitions of quasi-two-dimensional systems, in the melting transition as well as in registry–disregistry transitions.

The dominance of fluctuations in lower-dimensional systems can also be understood by simpler arguments. The order of a phase is thermodynamically determined by the free energy, i.e. by the competition between energy and entropy. In three-dimensional systems each atom has a large number of nearest neighbors (e.g. twelve in an f.c.c. crystal); thus the energy term stabilizes an ordered state, local fluctuation being of minor importance. In one dimension, however, each atom has only two nearest neighbors. Here the entropy term dominates the energy term, and even very small local fluctuations destroy the order. In a close-packed two-dimensional system each atom has six nearest neighbors and, depending on temperature, energy and entropy may be in balance. As amplitude fluctuations, i.e. topological defects, can be excited thermally, the two-dimensional systems seem to be ideally suited for studying defect-mediated phase transitions.

4.2. Soliton structure of incommensurate phases

4.2.1. Solitary lattice distortion waves

The essential properties of incommensurate modulated structures can be studied within a simple one-dimensional model, the well-known Frenkel–Kontorova model[60]. The competing interactions between the substrate potential and the lateral adatom interactions are modeled by a chain of adatoms, coupled with harmonic springs of force constant K, placed in a cosine substrate potential of amplitude V and periodicity b (see Fig. 27). The microscopic energy of this model is:

$$H = \sum_n \left[\frac{K}{2}(x_{n+1} - x_n - a_0)^2 \right] + \sum_n V \left[1 - \cos\left(\frac{2\pi}{b} x_n \right) \right] \tag{24}$$

where x_n is the position of the nth atom. In the absence of the periodic potential

($V = 0$) the distance between nearest-neighbor atoms in the chain is a_0, which, in general, is incommensurate with the substrate lattice constant b. Frank and van der Merwe[61] (FvdM) solved this model analytically within a continuum approximation. They replaced the index n by a continuous variable and x_n by a continuous function $\varphi(n)$. The calculations of FvdM showed that for slightly differing lattice parameters of chain and substrate potential, the lowest energy state is obtained for a system which consists of large commensurate domains, separated by regularly spaced regions of bad fit (Fig. 27). The regularly spaced regions of bad lattice fit are called misfit dislocations, solitons or domain walls. They can be regarded as collective long period lattice distortion waves, which are excitations of the commensurate ground state.

In the continuum approximation of FvdM the microscopic energy can be written:

$$H = \int \left[\frac{Kb^2}{8\pi^2} \left(\frac{d\varphi}{dn} - 2\pi\delta \right)^2 + V(1 - \cos(p\varphi)) \right] dn \tag{25}$$

where $\delta = (a_0 - b)/b$ is the natural misfit of the periodicites of the adatom chain and of the substrate potential, p the commensurability and $\varphi(n) = (2\pi x/b) - 2\pi n$ the phase shift of the chain atom with respect to the potential minimum.

The Hamiltonian, Eq. (25), can be minimized exactly. The ground state satisfies the time-independent sine Gordon equation:

$$\frac{d^2\varphi}{dn^2} = pA \sin(p\varphi) \tag{26}$$

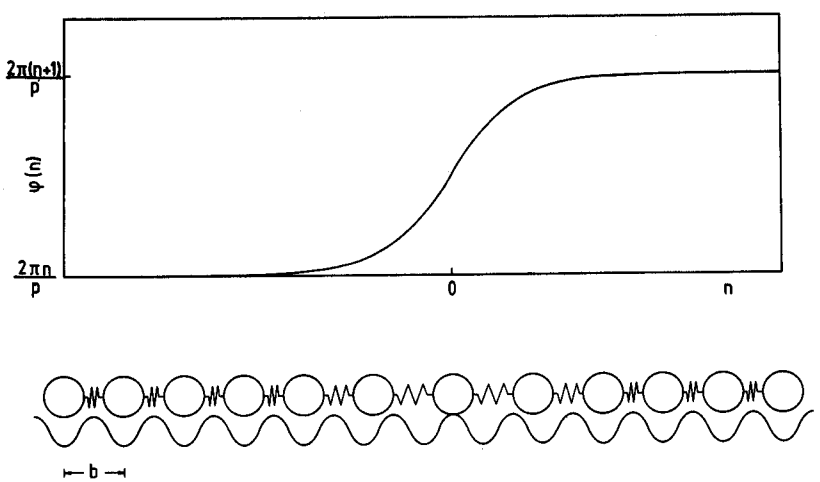

Fig. 27. Single soliton solution of the 1D Frank–van der Merve model of incommensurate monolayers.

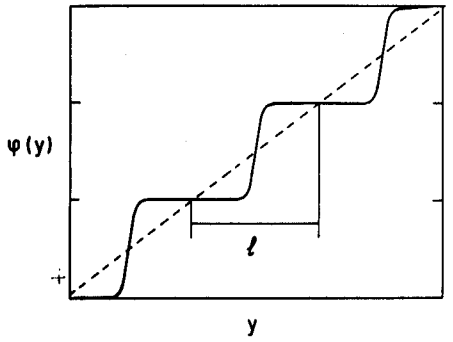

Fig. 28. Soliton lattice solution of the FvdM model with regularly spaced, distance l, domain walls. The dashed line corresponds to the incommensurate phase with negligible potential modulation ($V = 0$). The plateaus represent the commensurate domains.

with

$$\sqrt{A} = 2\pi/b\sqrt{V/K}$$

One solution of this equation is the solitary lattice distortion, the so-called soliton:

$$\varphi(n) = \theta(n) = \frac{4}{p}\arctan\left[\exp\left(pn\sqrt{A}\right)\right] \tag{27}$$

The soliton solution is shown in Fig. 27; it describes a domain wall located at $n = 0$ separating two adjacent commensurate regions. The width of the domain wall in this model is $L_0 = 1/(p\sqrt{A})$. In general, the solutions are regularly spaced solitons (Fig. 28). The distance between solitons, l, is determined by the lateral interaction between neighboring walls which is mediated by the lateral atomic displacements in the chain. At large distances from a wall, $\sin\varphi$ is small and Eq. (26) may be linearized, yielding an exponential decay. Therefore, the repulsive interaction between neighboring walls is also exponential. The phase function of the regularly spaced solitons have the functional form (Fig. 28)

$$\varphi = \varphi_0 + \frac{2\pi f}{p} + \theta(y - fl) \tag{28}$$

with f being the closest integer to y/l and $y = nb$.

4.2.2. The commensurate–incommensurate transition of monolayer Xe on Pt(111)

In two-dimensional systems, walls are lines with finite width. In a triangular lattice there are three equivalent directions. Therefore, domain walls can cross

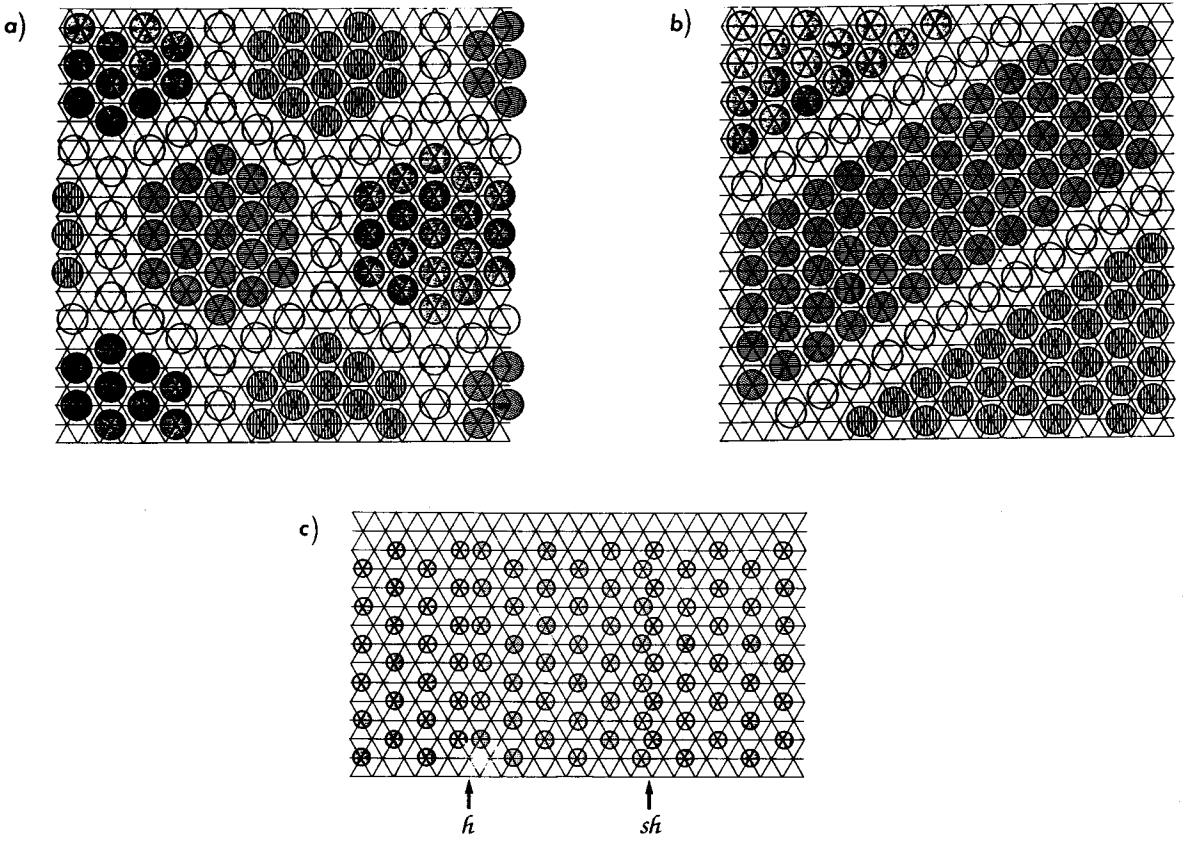

Fig. 29. Schematic diagrams showing (a) hexagonal and (b) striped domain wall arrangements (only superlight walls are drawn on a triangular lattice (e.g. the (111) face of f.c.c. metals)). In incommensurate layers, where the monolayer is compressed with respect to the commensurate lattice, domain walls or either heavy or superheavy (c).

(Fig. 29). Using Landau theory, Bak *et al.*[62] (BMVW) have shown that it is the wall crossing energy Λ which determines the symmetry of the weakly incommensurate phase and the nature of the phase transition:

1. $\Lambda < 0$, i.e. attractive walls. A hexagonal network of domain walls (HI) will be formed at the commensurate (C–I) transition, because the number of wall crossings tends to be as large as possible. This C–HI transition should be first order.
2. $\Lambda > 0$, i.e. repulsive walls. The number of walls tends to be as small as possible, i.e. a striped network of parallel walls (SI) will be formed in the incommensurate region. The C–SI transition should be continuous. The striped phase is expected to be stable only close to the C–I transition. At larger misfits the hexagonal symmetry should be recovered in a first-order SI–HI transition.

The FvdM as well as the BMVW model neglects thermal fluctuation effects; both are $T = 0$ K theories. Pokrovsky and Talapov[63] (PT) have studied the C–SI transition including thermal effects. They found that, for $T \neq 0$ K the domain walls can meander and collide, giving rise to an entropy-mediated repulsive force of the form $F \sim T^2/l^2$, where l is the distance between nearest neighbor walls. Because of this inverse square behavior, the inverse wall separation, i.e. the misfit m, in the weakly incommensurate phase should follow a power law of the form

$$m = \frac{1}{l} \sim \left(1 - \frac{T}{T_c}\right)^{1/2} \tag{29}$$

In a recent He diffraction study[64] we have shown that the adsorption system Xe/Pt(111) is dominated by the existence of a $(\sqrt{3} \times \sqrt{3})$ R30° commensurate phase, shown schematically in Fig. 30. The C-phase has been found to be stable in an extended temperature (62 K–99 K) and coverage range ($\theta_{Xe} \lesssim 1/3$).

The maximum coverage in this $(\sqrt{3} \times \sqrt{3})$ R30° commensurate structure is obviously $\theta_{Xe} = 1/3$ ($\theta_{Xe} = 1$ corresponds to 1.5×10^{15} atoms/cm^2, the density of Pt atoms in the (111) plane). Only one-third of the adsorption sites are occupied, i.e. there exist three energetically degenerate commensurate sublattices. The commensurate Xe lattice being expanded by about 9% with respect to the 'natural' Xe-lattice, the coverge can be increased beyond $\theta_{Xe} = 1/3$. Obviously, above this limit the adatoms cannot all occupy preferred adsorption sites, and the adlayer becomes incommensurate. Due to anharmonic effects[64], the Xe adlayer becomes incommensurate also at $\theta_{Xe} < 1/3$ upon decreasing the temperature below ≈ 62 K. This has been predicted for an analogous case, Kr/graphite, by Gordon and Villain[65], but has not yet observed experimentally in that case.

Before discussing the experimental results of the C–I transition of Xe on Pt(111) in detail, let us have a look at the diffraction patterns expected from a

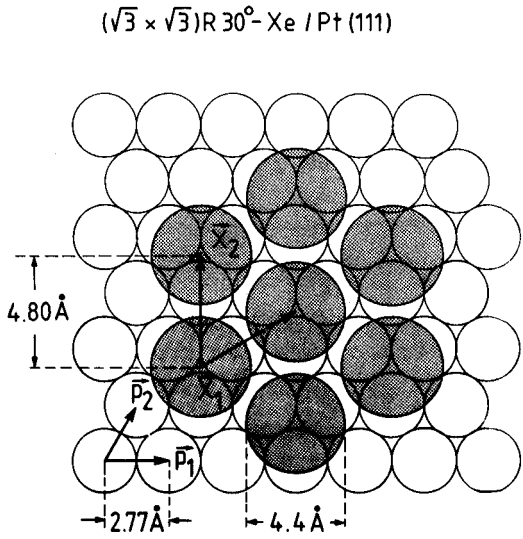

Fig. 30. Commensurate $(\sqrt{3} \times \sqrt{3})R30°$ Xe monolayer adsorbed on Pt(111).

striped (SI) and from a hexagonal incommensurate (HI) phase. The structure and the corresponding schematic diffraction patterns are shown in Fig. 31; the diffraction patterns have been calculated for fully relaxed walls, i.e. the SI and the HI phase are in fact uniaxially and uniformly compressed phases, respectively. By inspection of Fig. 31 it is obvious that the various incommensurate structures can easily be identified by their characteristic diffraction patterns.

We discuss first the basic crystallography of the incommensurate Xe phase on Pt(111) as deduced from the measured patterns[66]. Figure 32 shows the $(2,2)_{Xe}$ and $(1,2)_{Xe}$ diffraction features obtained from a Xe layer during the C–I transition induced by cooling below 62 K at constant coverage $\theta_{Xe} \simeq 0.30$. The plots have been obtained by monitoring series of azimuthal scans (i.e. constant Q scans in the reciprocal space). The comparison with Fig. 31 shows that the incommensurate Xe layer on Pt(111) is a striped phase (SI) with a uniaxial compression in the $\bar{\Gamma}\bar{M}$ direction. Indeed, a three-peak structure for the $(2,2)_{Xe}$ diffraction feature, with the doublet located at $Q^{2,2}_{comm} + 0.048\,Å^{-1}$ and the single peak located at $Q^{2,2}_{comm} + 0.90\,Å^{-1}$ is observed (with $Q^{2,2}_{comm} = 3.02\,Å^{-1}$); whereas the $(1,2)_{Xe}$ pattern consists of a single peak at the commensurate position and a shallow doublet with the maximum intensity at about $Q^{1,2}_{comm} + 0.13\,Å^{-1}$ (with $Q^{1,2}_{comm} = 2.62\,Å^{-1}$). The observed incommensurability deduced from the well-defined polar location of the peaks in Fig. 32a is $\varepsilon = 0.095$ Å and corresponds to an inter-row distance in the $\bar{\Gamma}\bar{M}$ direction of $d_{SI} = 3.91$ Å. This results in a misfit $m = 1 - d_{SI}/d_C = 0.059$, where $d_C = 4.80$

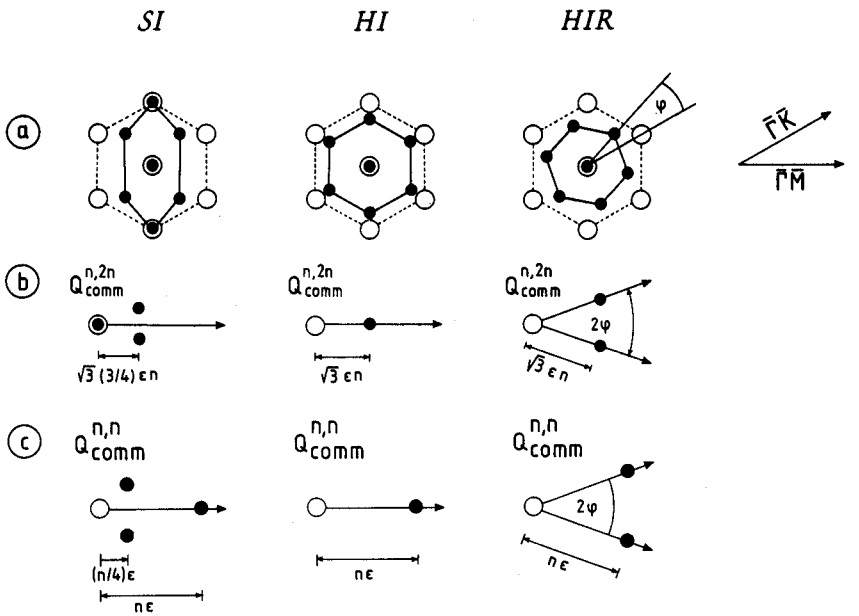

Fig. 31. Schematics of (a) real lattice and (b), (c) the (n, n) and $(n, 2n)$ diffraction features of incommensurate layers. SI – striped incommensurate, HI – hexagonal incommensurate, HIR – hexagonal incommensurate rotated. All phases are assumed to be fully relaxed. ○ denotes the $(\sqrt{3} \times \sqrt{3})$R30° commensurate and ● the incommensurate structures.

× cos 30° Å is the inter-row distance of the commensurate Xe structure in the same direction. From the measured polar and azimuthal peak widths in Fig. 32 we can also estimate average domain sizes of the incommensurate layer. For the $\bar{\Gamma}\bar{K}$ direction, i.e. parallel to the walls, we obtain ~ 350 Å and for the perpendicular $\bar{\Gamma}\bar{M}$ direction ~ 50 Å.

The analysis in the last paragraph has shown that the incommensurate Xe layer on Pt(111) at misfits of about 6% is a striped phase with fully relaxed domain walls, i.e. a uniaxially compressed layer. For only partially relaxed domain walls and depending on the extent of the wall relaxation and on the nature of the walls (light, heavy or superheavy) additional statellites in the (n, n) diffraction patterns should appear. Indeed, closer to the beginning of the C–I transition, i.e. in the case of a weakly incommensurate layer (misfits below ~ 4%) we observe an additional on-axis peak at $Q^{2,2}_{comm} + \varepsilon/2$ in the (2, 2) diffraction pattern. In order to determine the nature of the domain walls we have calculated the structure factor for the different domain wall types as a function of the domain wall relaxation[67] following the analysis of Stephens *et al*[68]. The observed additional on-axis satellite is consistent with the occurrence of superheavy striped domain walls; the observed peak intensities indicate a domain wall width of $\lambda \simeq 3$–5 Xe inter-row distances. With

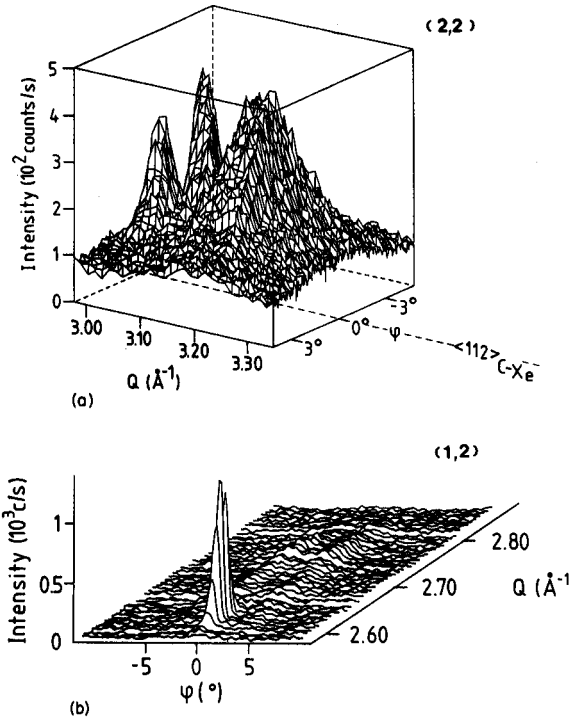

Fig. 32. 3D plot of (a) the $(2,2)_{Xe}$ and (b) the $(1,2)_{Xe}$ diffraction features during the C–I transition at $T = 54$ K ($\theta_{Xe} \approx 0.30$). Q denotes the wavevector in the $\bar{\Gamma}$ $\bar{M}$ and $\bar{\Gamma}$ $\bar{K}$ directions, respectively, while φ denotes the azimuthal angle.

increasing incommensurability the total length of the domain walls is expected to increase, giving rise to smaller and more numerous commensurate domains[69]. For misfits larger than 4–5%, i.e. where the interwall distance becomes less than three times the wall width, the diffraction pattern of the striped incommensurate layer can no longer be distinguished from an unaxially compressed layer.

In Fig. 33 the misfit during the temperature-induced C–I transition is plotted as a function of the reduced temperature. As long as the phase is weakly incommensurate the data can be fitted by a power law: $m = m_0(1 - T/T_c)^{\beta}$. The best least square fit parameters are $T_c = 61.7$ K, $m_0 = 0.18$ and $\beta = 0.51 \pm 0.04$. The value of β is in agreement with the Pokrovsky–Talapov prediction. Only data points up to misfits of about 4% have been included in the fit. The cutoff $\sim 4\%$ has been choosen in accordance with Erbil *et al.*[70], who have found the $\beta = 1/2$ power law to be valid only in this range for bromine intercalated graphite. For larger values, the misfit variation with reduced temperature is roughly linear; in this region the interwall distance is of

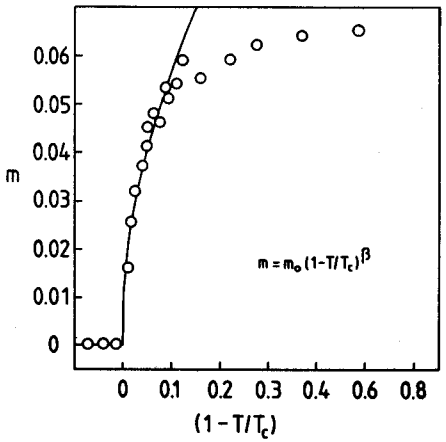

Fig. 33. $\bar{\Gamma}$ $\bar{M}$ uniaxial misfit m versus reduced temperature during the C–SI transition. The solid line represents the power law fit (see text).

order of the wall width and thus the Pokrovsky–Talapov theory is not applicable.

Due to the instability of the hexagonal weakly incommensurate phase with respect to the formation of free dislocations (re-entrant melting) the C–HI transition of Kr on graphite[71] (which like Xe/Pt(111) exhibits a $(\sqrt{3} \times \sqrt{3})$ R30° commensurate structure) has been found to be a melting transition. In contrast, the C–SI transition of Xe/Pt(111) is a solid–solid transition with the incommensurability simply related to the domain wall density. According to Coppersmith *et al.*[72] striped structures are stable if the number of sublattices, p (here, $p = 3$), is larger than $\sqrt{8}$, whereas for hexagonal structures the criterion is $p > 7.5 \pm 1.5$. As mentioned, the critical exponent $\beta = 0.51 \pm 0.04$ deduced from the data in Fig. 33 is in agreement with the $\beta = 1/2$ prediction of Pokrovsky and Talapov. The Pokrovsky–Talapov model may essentially be applied to a substrate of uniaxial symmetry; however, the original model calculations are performed for an isotropic substrate and thus applicable to the isotropic Pt(111) substrate. On the other hand, Haldane and Villain[73] pointed out that in the case of rare-gas monolayers on metal surfaces, substrate-induced electric dipole interactions might be responsible for the square root law. Moreover, they inferred that even in the case of an insulating substrate (no induced dipole forces) the square root behavior should be valid, but only for very small misfits ($m < 0.001$!). At present, it is difficult to make a choice between the thermal fluctuation mechanism of Pokrovsky and Talapov and the substrate-induced dipole mechanism of Haldane and Villain. However, it is worth noting that the experimental range of validity of the square root law in 2D striped domain

wall phases has been found to be actually much larger (a factor of ≈ 30) than the limit given by Haldane and Villain, for 'insulating' substrates (Br intercalated graphite[46]) as well as for metal substrates (Xe/Cu(110)[74], Xe/Pt(111).[66]

The direct implication of the existence of a striped phase in Xe layers on Pt(111) is that the wall-crossing energy is substantially positive. This is at variance with observations made for Kr layers on graphite[71], where the crossing energy was always found to be negative or at least only slightly positve (so that entropy gain due to the free breathing of the honeycomb lattice is sufficient to favor the hexagonal symmetry). Gooding *et al.*[75] have studied the influence of the substrate potential modulation on the different wall energies. They found that for large potential modulations striped arrays of discommensurations might have lowest energy. This goes along with the large potential modulation observed for the Xe/Pt(111) system[76]. The extended misfit range ($0 < m < 7.2\%$) in which the striped structure appears to be stable, is somewhat puzzling in view of recent theoretical results by Halpin-Healy and Kardar[77]. They have studied the occurrence of striped structures in the 'striped helical Potts lattice gas model'. Their results reveal a strong correlation between the extent of the striped phase regime and the wall thickness. Striped structures in an extended coverage range should appear only for 'sharp' domain walls; with increasing wall thickness this range is expected to shrink substantially. The energy cost due to the wall repulsion seems to be too large for thick walls. They conclude that the wall width of 4–5 inter-rows in Kr monolayers on graphite[78] might be responsible for the absence of a striped phase in this system. The wall width in Xe layers on Pt(111) is of the same size; the coverage range in which the striped phase is found to be stable corresponds in Halpin-Healy and Kardar's calculations to walls widths of 1–2 inter-rows.

When increasing the misfit of Xe monolayers on Pt(111) above 6.5% an additional an-axis peak at $Q_{\text{comm}}^{1,2} + \sqrt{3}\varepsilon$ appears in the (1, 2) diffraction spots (Fig. 34). This marks the transition from the striped to the hexagonal

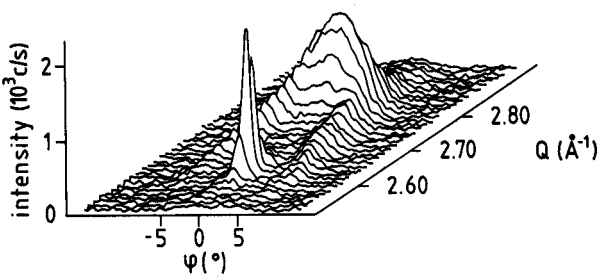

Fig. 34. 3D plot of the $(1,2)_{Xe}$ diffraction feature of an incommensurate Xe monolayer on Pt(111) at a misfit of 7.0% ($\Theta_{Xe} \simeq 0.35$, $T = 25$ K).

incommensurate phase. Such diffraction patterns composed of a peak at $Q_{comm}^{1,2}$ and a doublet at $Q_{comm}^{1,2} + (3/4)\sqrt{3}\varepsilon$ originating from a SI phase, and an on-axis peak at $Q_{comm}^{1,2} + \sqrt{3}\varepsilon$ originating from a HI phase, are observed in the misfit range $6.5\% \lesssim m \lesssim 7.2\%$, with the HI peak intensity progressively increasing with coverage. We conclude that the SI phase transforms at misfits of $\sim 6.5\%$ to a HI phase in a first-order transition.

Xe on Pt(111) appears to be the first 2D system fully consistent with the BMVW theory, i.e. the first system displaying the full sequence of C → SI → HI transitions with increasing incommensurability. Of course, the BMVW theory is a $T = 0$ K theory neglecting thermal fluctuation effects. However, Halpin-Healy and Kardar[79] have studied recently the various domain wall phases in the framework of a generalized helical Potts model, including finite temperature effects and two species of domain walls. Their results were in general agreement with the BMVW theory; in particular, they pointed out that the C → SI → HI sequence only occurs when assuming repulsive heavy and superheavy wall crossings. This is confirmed by the Xe/Pt(111) system.

4.2.3. The uniaxial soliton reconstruction of Au(111)

It is well known that all low-index clean gold surfaces exhibit reconstructions, in that the outermost layer has always a density larger than the corresponding bulk layers[55,56]. The genuinely rectangular (100) and (110)

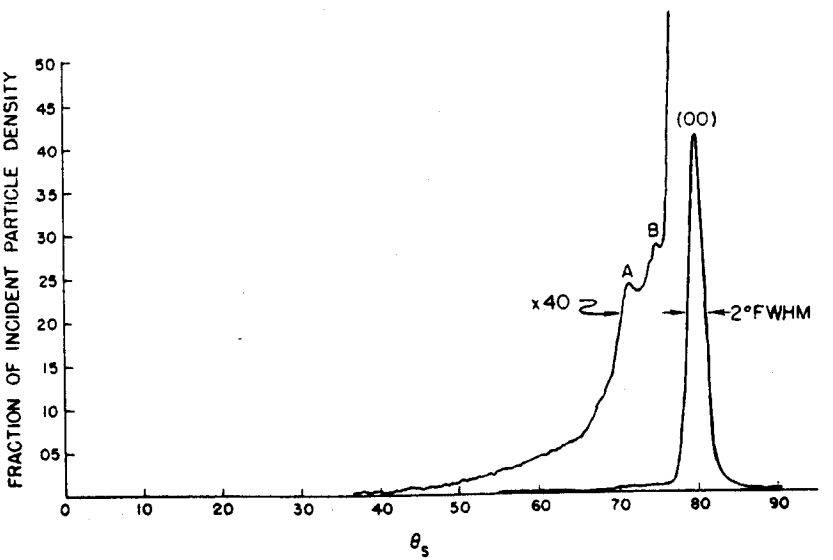

Fig. 35. He diffraction from Au(111) with a primary He beam energy $E_i = 11$ meV ($\vartheta_i = 80°$, $T_S = 145$ K). (*After Ref. 80.*)

outermost Au layers reconstruct to hexagonal close-packed structures, while on the Au(111) surface the density increases by a lateral contraction of the outermost atom layer.

The first experimental evidence for a uniaxial soliton reconstruction of the Au(111) surface was obtained in 1977 by Miller and Horne[80]; unfortunately, they missed the significance of the data. They scattered He beams with energies of 11–63 meV from Au(111) surfaces. Figure 35 shows a polar He diffraction scan with a beam energy of 11 meV, at a fixed incident angle $\vartheta_i = 80°$ obtained

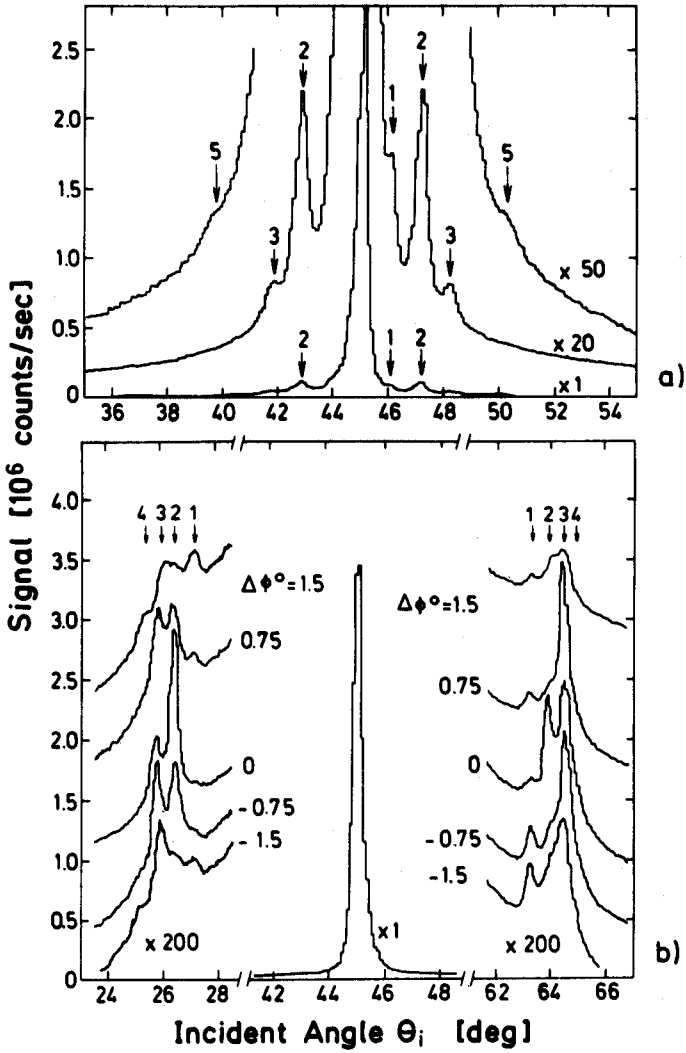

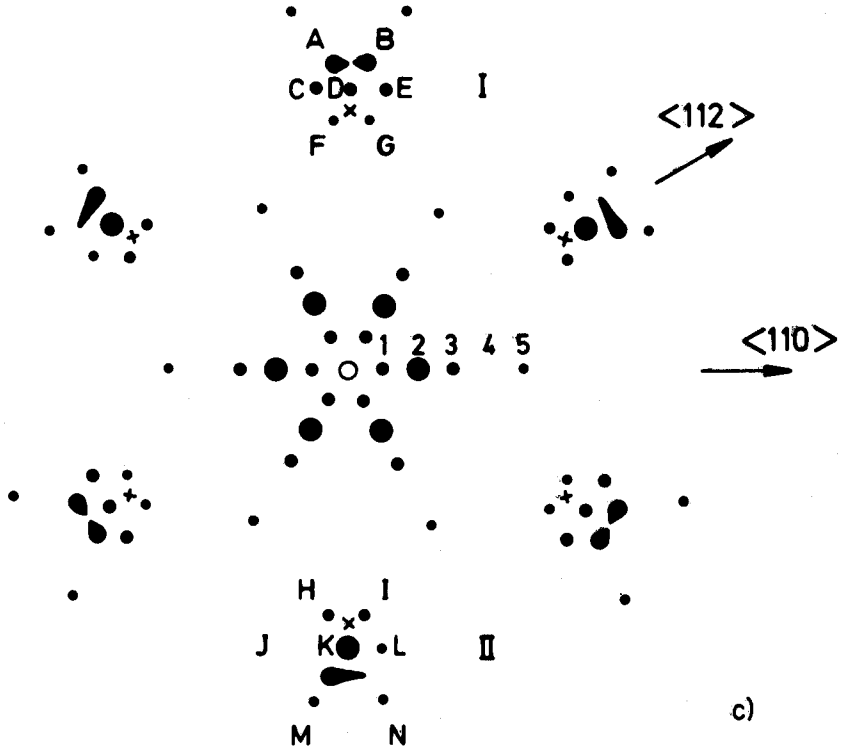

Fig. 36. He diffraction scans taken from Au(111) along (a) the $\bar{\Gamma}\,\bar{K}_{Au}$ azimuth ($E_i = 7.95$ meV) and (b) the $\bar{\Gamma}\,\bar{M}_{Au}$ azimuth ($E_i = 16.6$ meV). (c) Full diffraction pattern shown schematically. (*After Ref. 81.*)

by varying the scattering angle ϑ_f. Despite the relatively poor monochromaticity and angular resolution ($\Delta E/E \approx 0.2$ and angular divergence 0.8°) the polar profile shows two peaks, located at 71.4° (A) and 74.8° (B), corresponding to wavevectors $Q \approx 0.18\,\text{Å}^{-1}$ and $0.09\,\text{Å}^{-1}$. Miller and Horne assigned these peaks to single phonon exchanges between the He atoms and the Au surface.

In 1985 Harten *et al.*[81] repeated these measurements with better monochromaticity and angular resolution ($\Delta E/E \approx 0.02$ and angular resolution $\approx 0.3°$). Their results revealed up to five satellite peaks around the specular beam along the $\bar{\Gamma}\bar{K}_{Au}$ azimuth. Figure 36 shows polar He scans along the $\bar{\Gamma}\bar{K}_{Au}$ and $\bar{\Gamma}\bar{M}_{Au}$ azimuth, taken with beam energies of 7.95 meV and 16.6 meV, respectively. In the $\bar{\Gamma}\bar{K}_{Au}$ scans (a), the satellite peaks are located at wavevectors $Q_n \simeq n0.098\,\text{Å}^{-1}$, with a particularly strong second-order ($n = 2$) peak. This corresponds to a super-periodicity of ≈ 64 Å. This is very close to the value of the reconstruction model given by Takayanagi and Yagi[82]. Note that the peaks 1 and 2 of Harten *et al.*[81] are the peaks A and B in the notation

of Miller and Horen[80]. Along the $\bar{\Gamma}\bar{M}_{Au}$ azimuth, around the principal reciprocal lattice vector, a complicated diffraction pattern was observed (Fig. 36b, c).

From the position of the satellites in the $\bar{\Gamma}\bar{K}_{Au}$ azimuth, Harten *et al.* conclude that the Au(111) surface exhibits a regular soliton superstructure in that direction; the 23-fold periodicity corresponds to an average uniaxial compression of $\sim 4\%$. The characteristic peak splitting observed for the principal lattice vector in the $\bar{\Gamma}\bar{M}_{Au}$-direction indicates that the uniaxial compression is not distributed uniformly over the layer, but localized in narrow regions in the form of misfit dislocations. In the framework of a hard corrugated wall diffraction calculation (eikonal approximation), Harten *et al.* obtained the best fit for a model in which the soliton along the $\bar{\Gamma}\bar{K}_{Au}$-direction is produced by changing stacking from ABC (f.c.c. packing) to ABA (h.c.p. packing). In their model, the transition between the ABC and ABA regions is described by a continuous shift in position, according to the soliton solution of the FvdM model in Eq. (27). Based on transmission electron microscopy data, a rather similar model for the Au(111) reconstruction was proposed in 1982 by Takayanagi and Yagi[82]. A recent quantitative analysis of LEED data favors a similar reconstruction model[83].

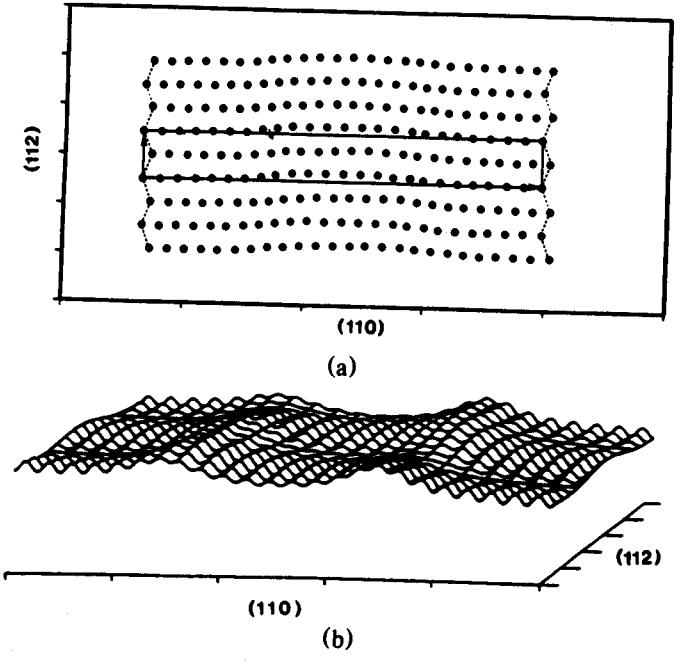

Fig. 37. (a) Atomic arrangement (top view) of the Au(111) surface atoms in the double sine Gordon model, (b) corrugation of the corresponding unit cell. (*After Ref. 84.*)

TABLE 3
Surface energy of reconstructed Au(111) surfaces according to the 'glue model' of Ercolessi *et al.*[85].

Surface arrangement	Surface energy (meV Å^{-2})
Au(111) bulk, unrelaxed	105.1
Au(111) relaxed, non-reconstructed	96.1
Au(111) $(7 \times \sqrt{3})$	90.4
Au(111) $(11 \times \sqrt{3})$	88.1
Au(111) $(23 \times \sqrt{3})$	90.2

El-Batanouny *et al.*[84] have recently analyzed the He diffraction data of Harten *et al.* in a refined soliton model. For the Au(111) surface, the A and C sites are not expected to be degenerated; a continuation of the Au-bulk structure would favor C-sites. To account for this nondegeneracy, El-Batanouny *et al.* have introduced the double-sine Gordon (DSG) equation to model the Au(111) reconstruction. Using molecular dynamics techniques they have solved this model and obtained an atomic arrangement of the surface atoms shown in Fig. 37. Hard corrugated wall diffraction calculations based on this atomic arrangement agree well with the experimental data.

The reconstruction of the Au(111) surface has also been subject to theoretical studies. Ercolesi *et al.*[85] have explored the reconstruction in a phenomenological many-body Hamiltonian, an approach which is known as the 'glue model'. In this model, the many-body forces minimize classically the non-directional cohesive forces of the filled d-bands, appearing as the main term in enforcing optimal coordination of all atoms. The procedure is empirical in nature and adjusted to reproduce the macroscopic properties of solid and liquid gold, as well as surface formation energies. The optimum structure of the surface is obtained by an 'annealing' procedure based on molecular dynamics techniques. Within this model, the (111) surface of gold does exhibit reconstruction. In qualitative agreement with the experiment, the surface energy is minimized by a soliton-like reconstruction, with a smooth transition from f.c.c. to h.c.p. stacking, with a unit cell length of $(L \times \sqrt{3})$. However, in contrast to the experimental findings ($L = 23$) the theoretical optimal value is $L = 11$ (see Table 3).

4.3. Surface reconstruction and soft phonons, W(100)

A basic concept in the reconstruction theory of solid surfaces is the soft phonon approach of displacive structural transitions. An essential property of these structural phase transitions is the existence of an order parameter which

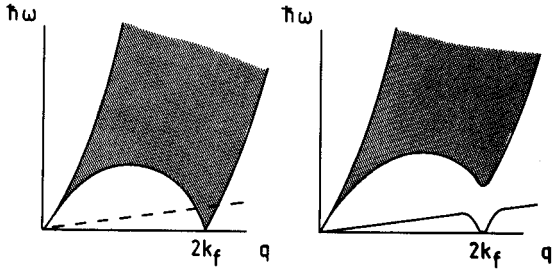

Fig. 38. 1D model of metal surface reconstruction. The coupling between discrete phonon modes (dashed line) and the electron–hole pair continuum (hatched) produces lattice instability.

represents a collective displacement of the atoms. At the reconstructive transition the surface lattice distorts via the softening of the corresponding phonon (the order parameter diverges), i.e. the configuration of atomic displacements changes continuously during the transition.

Several authors have suggested that these lattice instabilities may arise as a result of 'giant Kohn anomalies'[86,87]. The electronic energy of a metal surface may be lowered by periodic lattice distortion waves of wavevector $Q_{\mathrm{LDW}} = 2k_{\mathrm{f}}$, where k_{f} is the Fermi wavevector of the surface electrons. This is exemplified in Fig. 38 where the continuum of electron–hole pair excitations $\omega(q)$ with its characteristic low-energy regime around the Fermi vector is shown. The dashed line represents a longitudinal surface phonon. The phonon vibrations couple to the electrons for coincident phonon and electron–hole pair creation, giving rise to a mode repulsion which depresses the phonon energy near $2k_{\mathrm{f}}$ and creates a gap in the electron–hole pair band. In the case of sufficient coupling strengths, the phonon frequency becomes zero and the surface can reconstruct by freezing this particular lattice distortion.

The strength of the lattice instability near the Fermi vector depends on the magnitude of the electron–phonon coupling and on the phase space available for electron–hole pair excitation around $2k_{\mathrm{f}}$. Thus, a reconstructive surface phase transition has to fulfill the following requirements in order to be ascribed to an electronically driven lattice instability:

1. Surface states or resonances have to be present near the Fermi energy in the electronic surace band structure.
2. The Fermi surface must have large regions of flat parallel areas, i.e. it must exhibit strong nesting properties.
3. The symmetry of the electronic surface bands has to allow for strong electron-phonon coupling to distortions of appropriate symmetry.

The W(100) surface is suspected to be a representative for this kind of

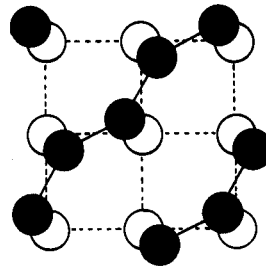

Fig. 39. Schematics of the W(001) p2mg surface reconstruction; the Debe–King model.

electronically driven reconstructions. Already in 1971 Yonehama and Schmidt[88] observed with LEED that the clean W(100) reconstructs upon cooling below room temperature. At low temperature, the reconstructed surface exhibits a sharp $c(2 \times 2)$ LEED pattern, i.e. extra Bragg spots in the (1/2, 1/2) position, which become weak and diffuse upon approaching the transition temperature.

A qualitative structural model of the reconstructed $c(2 \times 2)$ W(100) surface was first proposed by Debe and King[89] on the basis of symmetry arguments. Figure 39 shows this reconstruction model. The surface atoms exhibit only in-plane displacements along diagonal directions. A subsequent LEED structurel analysis of Barker *et al.*[90] supported this picture. In a more recent quantitative LEED analysis, Walker *et al*[91] deduced a lateral displacement of 0.16 Å at 200 K.

More recently, the reconstruction of the clean W(100) surface has also been studied by He diffraction[92,93]. These studies reveal a complex behavior during the transition. Only at temperatures below ~ 240 K sharp diffraction spots *centered* at the (1/2, 1/2) positions are observed. In the temperature range between ~ 400 K and ~ 240 K broad superstructure spots are observed which progressively shift to the (1/2, 1/2) position upon cooling. Lapujoulade and Salanon[92] explain this behavior in the framework of a domain wall model: reconstructed domains of various sizes are separated by dense domain walls, which disappear continuously upon cooling.

Detailed electronic energy-band calculations[94] have revealed the existence of appropriate surface states near the Fermi energy, indicative of an electronically driven surface instability. Angle-resolved photoemission studies, however, showed that the Fermi surface is very curved and the nesting is far from perfect[95]. Recently Wang and Weber[96] have calculated the surface phonon dispersion curve of the unreconstructed clean W(100) surface based on the first principles energy-band calculations of Mattheis and Hamann[94].

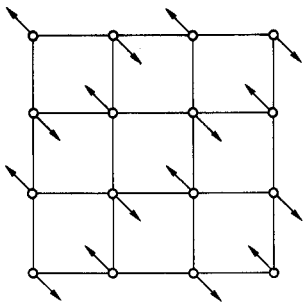

Fig. 40. Displacement pattern of the W(100) $\bar{M}_5$ surface phonon.

They found a whole bunch of soft phonons, which are primarily horizontally polarized, near the zone boundaries between $\bar{M}$ and $\bar{X}$. The most unstable mode they observed is the $\bar{M}_5$ phonon, the displacement pattern of which is shown in Fig. 40; note the similarity between this pattern and the reconstruction model in Fig. 39. According to Wang and Weber, these soft phonons are caused by electron–phonon coupling between the surface phonon modes and the electronic $\bar{\Sigma}_2$ surface states at the Fermi surface. They attributed the predominant M_5 phonon instability to an additional coupling between $d(x^2 - y^2)$ and $d(xy)$ orbitals of the Σ_2 states.

The $\bar{M}_5$ phonon instability as the cause of the $c(2 \times 2)$ reconstructionwas also predicted in the pioneering work of Tosatti and coworkers[97] and in a more recent 'frozen phonon' total energy calculation of Fu *et al.*[98]. In the approach of Tosatti *et al.* the reconstruction mechanism is treated by incorporating the electronic driving forces in extra forces between surface atoms, i.e. studying the reconstruction essentially as a lattice dynamical problem by introducing empirical force constants between nearest neighbors. For values of the surface force constants, corresponding to increased lateral attraction in the surface plane, the $\bar{M}_5$ phonon frequency becomes imaginary, i.e. the W(100) surface can reconstruct via the observed lattice distortion. In contrast to the Wang–Weber model, which includes long-range interatomic interactions, the model of Tosatti *et al.* is based on the short-range nature of the interaction.

More recently, Ernst *et al.*[93] have studied the surface phonon dispersion of W(100) along the $\bar{\Gamma}\bar{M}$-azimuth by means of high-resolution inelastic He scattering. Besides the Rayleigh phonon, they observed an additional acoustical low-frequency mode. This mode resulted in rather broad energy losses in the He time-of-flight spectra and has an unusual dispersion. Its energy increases initially with increasing wave-vector, reaches a maximum at about 2/5 of the Brillouin zone and softens upon further increase of the wavevector; it

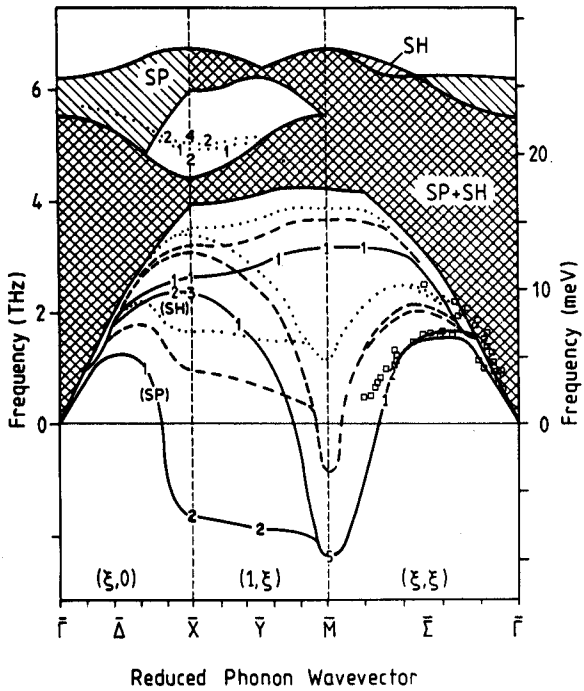

Fig. 41. Surface phonon dispersion of the unreconstructed W(100) surface. The theoretical dispersion curves are from Ref. 96; the data (□) are due to Ernst *et al.*[93].

eventually reaches zero energy near the zone boundary. Upon lowering the temperature, i.e. initiating the reconstruction, the Rayleigh mode does not change, while the soft phonon mode lowers slightly its energy. This behavior is consistent with the assertion that the soft mode is an in-plane mode, which might be connected with the reconstruction mechanism. Indeed, the Rayleigh mode being a vertical mode, we expect neither an anomalous dispersion nor a softening, because these forces are not important in driving the reconstruction. In Fig. 41 we have included the experimental data of Ernst *et al.*[93] in the theoretical dispersion curve of Wang and Weber[96]; the agreement between experiment and theory is reasonable.

4.4. Surface roughening

In their pioneering work on crystal growth Burton, Cabrera and Frank[99] predicted that on an atomic length scale the equilibrium structure of a crystal surface should exhibit a transition from a smooth state at low temperatures to

a rough surface at higher temperatures. The critical temperature of this transition has been termed the roughening temperature, T_R. Burton *et al.* suggested that at the roughening temperature the free energy associated with the creation of a step vanishes[99]. This was confirmed later by Swendsen[100] in a detailed calculation. One of the fundamental consequences of the existence of a roughening temperature for a certain crystallographic face below the melting temperature is that this face can occur on an equilibrium crystal only at temperatures below T_R.

Let us consider a surface which at $T = 0$ K is perfectly flat. Upon raising the temperature, thermal fluctuations give rise to vacancies, adatoms atoms and steps in the surface layer. The number of these 'defects' increases until, at the roughening temperature, the long-range order of the surface disappears. Long-range order is confined here to the 'height-correlation function' and not to the positional correlation function. Indeed, even above the roughening temperature, the surface atoms populate in average regular lattice sites. It is the fluctuation of the height $h(r)$ which diverges for temperatures $T > T_R$[101,102]:

$$\langle [h(\vec{r}') + \vec{r}) - h(\vec{r})]^2 \rangle \propto C(T) \ln(\vec{r}) \tag{30}$$

where C is a temperature-dependent constant and $\vec{r}$ a two-dimensional vector in a plane parallel to the surface. This divergence is very weak. At the roughening temperature $C(T_R) = 2/\pi^2$ [102]; the height fluctuation is one lattice spacing for a distance of 139 lattice spacings.

The roughening transition has also been studied by computer simulation methods[103]. Figure 42 shows characteristic configurations of a f.c.c. (100) surface in the simple solid-on-solid (SOS) model, calculated by Gilmer[103]. The roughening temperature in this model corresponds to a parameter $kT/\Phi = 0.6$.

The first indication for the existence of a roughening transition was obtained by Jackson and Miller[104] who studied the crystal shape of chloroethane and ammonium chloride. Above 370 K and 430 K, respectively, they observed a drastic change in crystal morphology, which might be interpreted as roughening. Similar observations for adamantane have been reported by Pavlovska[105].

The first first direct experimental evidence for a roughening transition was reported in 1979. Several groups[106,107] have studied the thermal behavior of the basal plane of a hexagonal close-packed ^{4}He crystal. In a beautiful experiment Balibar and Casting[108] obtained for this surface a roughening temperature of $T_R \approx 1.2$ K.

More recently, the question of thermal roughening has also been addressed in the study of metal surfaces. Detailed He diffraction studies from the high Miller index (115) surface of Cu and Ni proved the existence of a roughening transition on these surface. These studies were performed by means of He scattering. Let us make first two short comments.

The microscopic mechanism which leads to the roughening of a low and a

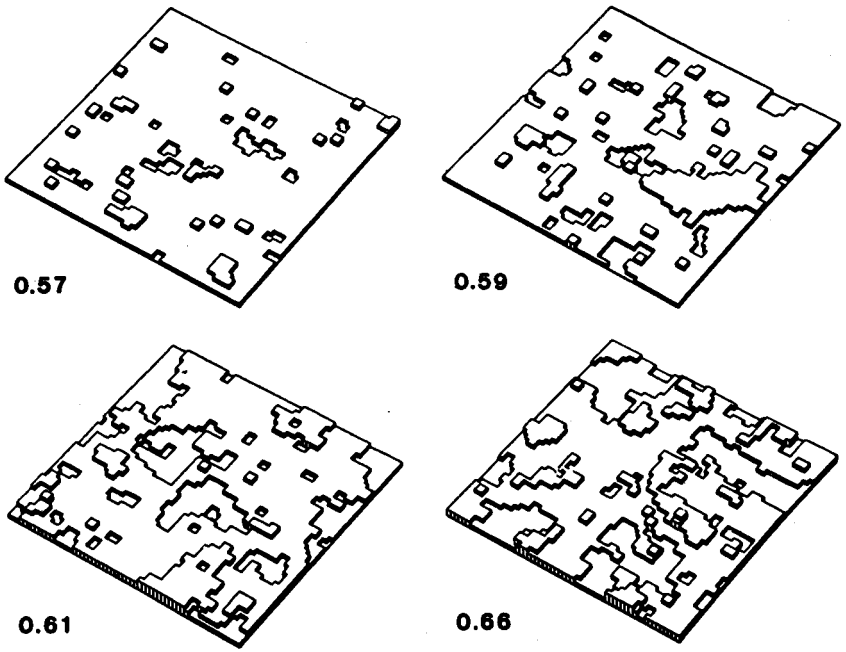

Fig. 42. Typical equilibrium configurations of a f.c.c. (100) crystal in the SOS model. (*After Ref. 103.*)

high Miller index surface is expected to be essentially different. Indeed, as already mentioned, a low indexed surface – which at $T = 0$ K is perfectly flat – fulfills the roughening condition, Eq. (30), when the free energy for the creation of a step becomes zero. In contrast, on a high indexed surface – which at $T = 0$ K is already stepped – Eq. (30) can be fulfilled also without the creation of new steps. It appears that the proliferation of kinks is sufficient to roughen the surface (Fig. 43). Indeed, the ensuing meandering of the step rows, in conjunction with the mutual repulsion between these rows, leads also to the divergence of the 'height-correlation function'. Thus, the roughening temperature of high indexed surfaces might be substantially lower than that of the low indexed ones.

Most studies of metal surface roughening have been performed with He scattering because two specific features make this probe particularly suited for the study of the roughening of single crystal surfaces:

1. Due to the large total cross-section of defects (about 150 Å^2 for a monovacancy on Pt(111)) He scattering is extremely sensitive to the presence of defects. In addition, this large cross-section enables one to study the lateral distribution of defects[6].

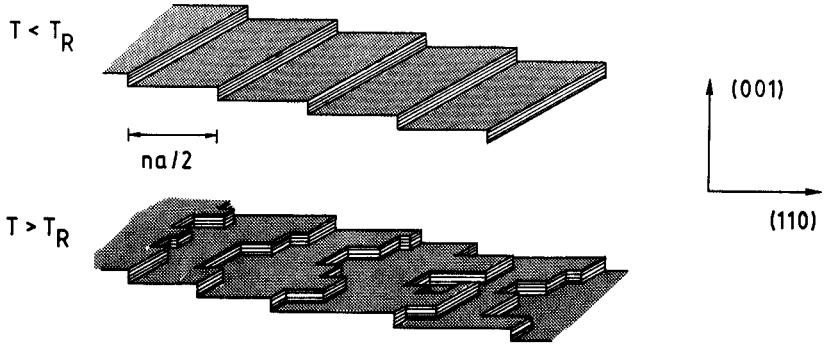

Fig. 43. Schematic sketch of a f.c.c. (11*n*) surface above and below the roughening temperature.

2. The interference between He particle waves scattered from adjacent terraces, separated by a monatomic step, provide detailed information about the step density and even about the actual distribution of terrace widths[109].

The first piece of evidence that a roughening transition might occur on single crystal metal surfaces was reported in 1982 by Lapujoulade *et al.*[110]. They observed a dramatic drop in the He intensities coherently scattered from the Cu(115) surface upon increasing the temperature above ~ 400 K (Fig. 44). This behavior contrasted with the generally observed, much weaker decrease of the coherent intensity, accounted for by the Debye–Waller factor[111]. Lapujoulade and coworkers claimed that this anomalous behavior was due to thermal roughening and assigned the temperature at which the data deviate from the Debye behavior to the roughening temperature. Such anomalous behavior, however, may have other causes (see below), but this assignment happened to be correct.

More sound experimental arguments for the existence of a roughening transition of high Miller index surfaces were reported three years later both by Engel's and Lapujoulade's groups[112–114]. In these studies, the thermal behavior of the He diffraction peak line shapes have been analyzed in the framework of simple roughening models, developed by den Nijs *et al.*[115] and by Villain *et al.*[116] Since the height correlation disappears when approaching T_R and since the diffraction intensity is simply related to the pair correlation function, the diffraction peak shape is expected to undergo characteristic changes at the roughening transition. Both theoretical models predict power-law lineshapes for the He diffraction peak. In particular, for the tail of the specular (0, 0) peak they infer that

$$I(Q_\parallel) \propto Q_\parallel^{\eta} \tag{31}$$

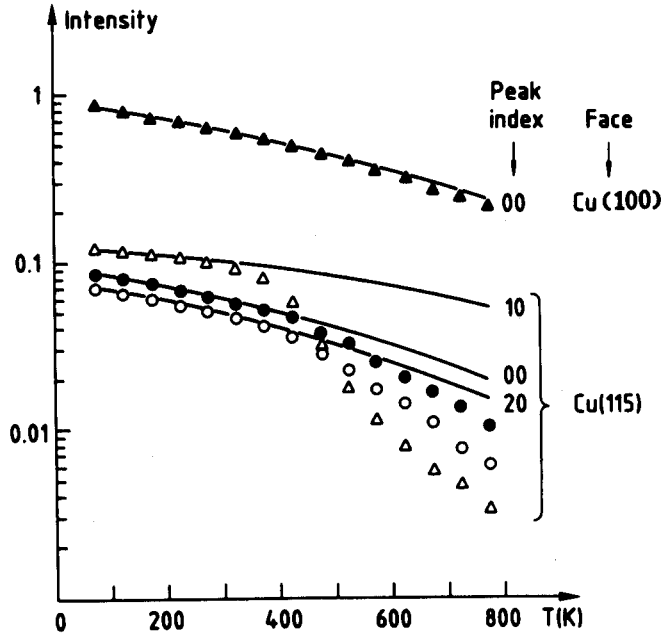

Fig. 44. Thermal dependence of coherently diffracted He intensities from Cu(100) and Cu(115). (*After Ref. 112.*)

with $\eta = (2x_R - 2)$, $Q_\parallel$ being the parallel momentum transfer and x_R the so-called roughening exponent. In the non-roughened state of the surface, the roughening exponent is expected to be $x_R = 0$ ($\eta = -2$), while it takes a value $x_R = 1/2$ ($\eta = -1$) at T_R and increases further with the temperature above T_R. We should note that this dependence is expected to be valid for elastic scattering only; the influence of inelastic scattering on the diffraction lineshape has not been considered so far in theory. Since the roughening temperature usually occurs well above the surface Debye temperature, inelastic phonon scattering strongly influences the lineshape, and has to be accounted for. In the study of Ni(115) and Ni(113), Conrad *et al.*[113,117] have corrected for this inelastic influence.

In Figs. 45 and 46 we summarize the results obtained by these authors for the Ni(115) and Ni(113) surface. Figure 45 shows the peak width (FWHM) of the specular He beam scattered from the Ni(115) surface along the $(\bar{5}, \bar{5}, 2)$ azimuth as a function of the incident angle θ_i. The oscillation characterizes the step density. The lineshapes of the specular He peak are shown in Fig. 46 in a log-log plot for Ni(113) along the $(\bar{3}, \bar{3}, 2)$ direction with the temperature as parameter. The profiles suggest the expected power-law behavior and the variation of the power exponent η (i.e. the slope) with temperature is obvious.

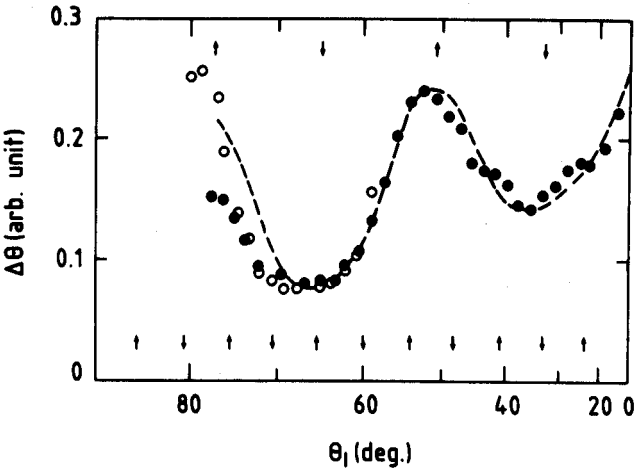

Fig. 45. Specular peak width (FWHM) vs incident angle for He scattering from Ni(115). (*After Ref. 113.*)

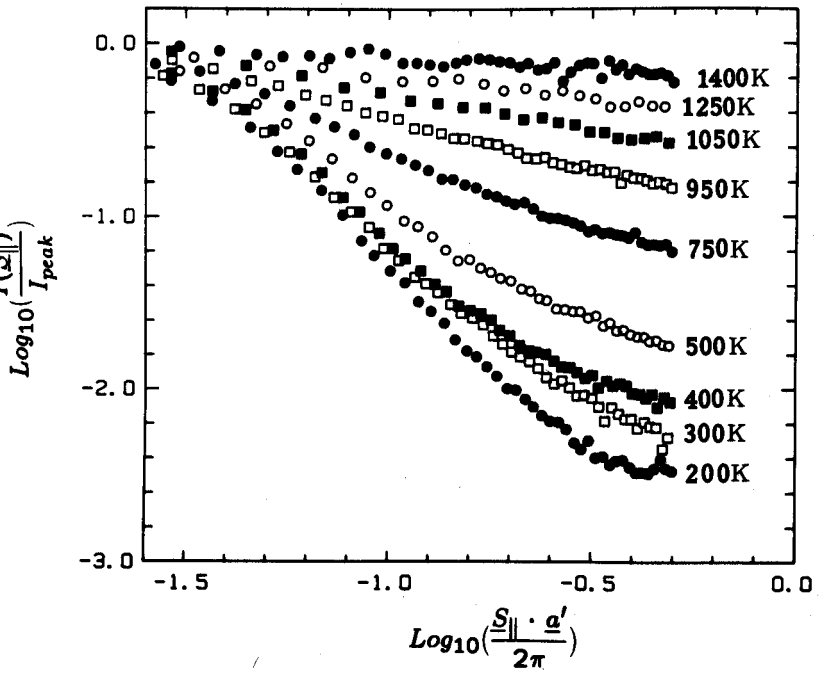

Fig. 46. Double-logarithmic plot of the lineshapes of the specular He intensity from a Ni(113) surface along the $(\bar{3}, \bar{3}, 2)$ direction with the temperature as parameter. (*After Ref. 117.*)

The data being obtained with an energy integrating detector, Conrad *et al.* tried to account for inelastic effects, by assuming a wave vector-independent multiphonon scattering and a one-phonon scattering probability proportional to $Q_{\parallel}^{-1}$. Then the roughening temperature was obtained from the corrected data via the roughening exponent $x_R = 1/2 \rightarrow \eta = -1$ at T_R. For the (113) surface of Ni they deduced a value of $T_R \approx 750 \pm 50$ K and for the (115) surface of the same metal they obtained $T_R \approx 450 \pm 50$ K. By using a somewhat similar procedure Lapujoulade and coworkers analyzed the (113) and (115) surface of Cu, obtaining roughening temperatures of 720 ± 50 K and 380 ± 50 K, respectively. The observed decrease of T_R with increasing terrace width is in agreement with the microscopic roughening mechanism of high indexed surfaces mentioned above. Indeed, in view of their mutual repulsion, it is easier for the step rows to meander when they are further apart.

The data analysis in the work of Conrad *et al.* and Lapujoulade *et al.* relies on statistical mechanical models assuming power-low lineshapes for the He diffraction peaks. In particular they assume a power exponent $x_R = 0 \rightarrow \eta = -2$ for a perfect flat surface. We have recently studied the lineshape of the specularly scattered He peak from an almost ideal (less than 0.1% defects) Pt(111) surface at low temperatures. By using energy-resolved He scattering, we were able to discriminate directly between purely elastic scattered atoms and those which have undergone an inelastic event, and thus to avoid more or less justified corrections. A log-log plot of the lineshape of the purely elastic component of the specular beam obtained with an 18 meV incident beam and a Pt surface temperature of 110 K is shown in Fig. 47. The data show the characteristic power-law behavior, but with the unexpected exponent $\eta \simeq -2.76$. Practially the same value for η ($\simeq -2.86$) has been observed also in the case of Cu(110). We have yet no explanation for this unusual exponent, but it raises at least some questions concerning the analysis of He scattering data measured without energy discrimination.

The discussion on the experimental evidence for the existence of roughening on low indexed surfaces is not yet settled. Let us consider for example the Cu(110) surface. More than ten years ago it had been noticed that the intensities in the photoemission spectra taken from Cu(110) decrease rapidly with temperature above ~ 500 K[118]. Similar effects have been seen recently in low-energy ion scattering[119], in X-ray diffraction[120] and in thermal He scattering[110,121]. The dramatic intensity decrease observed in all cases above 450–500 K could not be accounted for by simple Debye–Waller effects. While Lapujoulade *et al.*[110] and Fauster *et al.*[119] proposed as explanation either anharmonic effects or some kind of disorder, Mochrie[120] concluded categorically – without qualitative additional evidence – that he was observing the roughening transition. He even tentatively identified the temperature at which 'the intensity has fallen essentially to zero' (870 K) with T_R. A He specular intensity measurement on Cu(110) versus temperature performed in

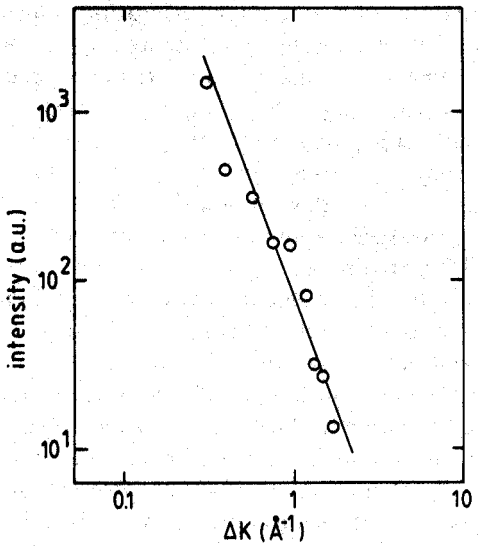

Fig. 47. Double-logarithmic plot of the lineshape of the purely elastic specular He intensity from a Pt(111) surface along the $\bar{\Gamma}\,\bar{M}$ azimuth. The primary beam energy was 18.3 meV.

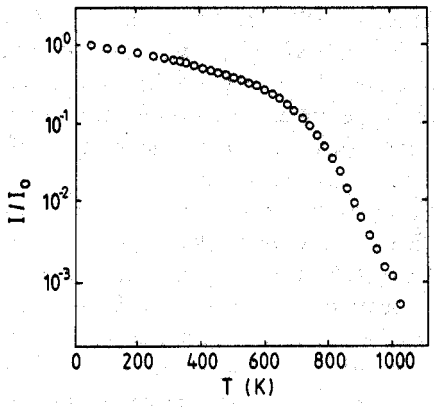

Fig. 48. Thermal dependence of the He specular peak height from Cu(110). The primary beam energy was 18.3 meV, and $\theta_i = \theta_f = 45°$.

our laboratory shows (Fig. 48) that also above 870 K the intensity continues to drop (at 1000 K it is already one order of magnitude lower) and that there is no sign of saturation even above 1000 K. Whether the intensity becomes 'essentially zero' appears to depend on the dynamical range of the instrument,

and is not a criterion for the choice of value of T_R. Zeppenfeld *et al.*[121] have analyzed very recently in detail the energy distribution of the scattered He atoms in the whole temperature range up to 1000 K. The various scattering components (elastic, one phonon and multiphonon) were clearly discriminated. The analysis shows that the anomalous intensity drop above ~ 500 K can be ascribed to multiphonon interactions, i.e. the strong increase of the mean square wave displacement of the surface atoms. Thus, the intensity drop is due to the enhancement of the anharmonicity and not necessarily to topological effects (no roughening up to 1000 K).

Acknowledgements

We are indebted to many colleagues all around the world, who by their contributions, lectures and discussions helped us to put together this review; especially to those who have accepted the reproduction of their results. We are particularly grateful to Rudolf David, Bene Poelsema and Peter Zeppenfeld for their decisive contribution to the developments originating in this laboratory. For illuminating discussions we wish to thank in particular to Harald Ibach and Jaques Villain.

For the typing and retyping to always new changes of the manuscript we are very much indebted to Maria Kober.

References

1. Johnson, T. H., *Phys. Rev.*, **37**, 847 (1931).
2. Engel, T., and Rieder, K. H., *Springer Tracts in Modern Physics*, Vol. 91, Springer, Berlin, 1982.
3. Kern, K., David, R., Palmer, R. L., and Comsa, G., *Phys. Rev. Lett.*, **56**, 2823 (1986).
4. Lahee, A. M., Manson, J. R., Toennies, J. P., and Wöll, Ch., *Phys. Rev. Lett.*, **57**, 471 (1986).
5. Frenken, J. W., Toennies, J. P., and Wöll, Ch., *Phys. Rev. Lett.*, **60**, 1727 (1988).
6. Comsa, G., and Poelsema, B., *Appl. Phys.*, **A38**, 153 (1985); Poelsema, B., and Comsa, G., *Springer Tracts in Modern Physics*, to be published.
7. Kern, K., David, R., and Comsa, G., *Rev. Sci. Instr.*, **56**, 369 (1985).
8. David, R., Kern, K., Zeppenfeld, P., and Comsa, G., *Rev. Sci. Instr.*, **57**, 2771 (1986).
9. Sköld, K., *Nucl. Instr. Meth.*, **63**, 114 (1968).
10. Comsa, G., David, R., and Schumacher, B. J., *Rev. Sci. Instr.*, **52**, 789 (1981).
11. Verheij, L. K., and Zeppenfeld, P., *Rev. Sci. Inst.*, **58**, 2138 (1987), and references therein.
12. Allen, R. E., Aldredge, G. P., and de Wette, F. W., *Phys. Rev.*, **B4**, 1661 (1971).
13. Lord Rayleigh, *Proc. London Math. Soc.*, **17**, 4 (1887).
14. Matthews, H., *Surface Wave Filters*, Wiley, New York, 1977.
15. Ho, K. M., and Bohnen, K. P., *Phys. Rev. Lett.*, **56**, 934 (1986).
16. Finnis, M. W., and Heine, V., *J. Phys.*, **F4**, L37 (1974).

17. Smoluchowski, R., *Phys. Rev.*, **60**, 661 (1941).
18. Jiang, P., Marcus, P. M., and Jona, F., *Solid State Communications*, **59**, 275 (1986), and references therein.
19. Badger, R. M., *J. Chem. Phys.*, **2**, 128 (1934); **3**, 710 (1935).
20. Baddorf, A. P., Lyo, I. W., Plummer, E. W., and Davis, H. L., *J. Vac. Sci. Technol.*, **A5**, 782 (1987).
21. Copel, M., Gustafsson, T., Graham, W. R., and Yalisove, S. M., *Phys. Rev.*, **B33**, 8110 (1986).
22. Baddorf, A. P., and Plummer, E. W., to be published.
23. Manson, J. R., and Celli, V., *Surf. Sci.*, **24**, 495 (1971).
24. Weare, J. H., *J. Chem. Phys.*, **61**, 2900 (1974).
25. Brusdeylins, G., Doak, R. B., and Toennies, J. P., *Phys. Rev. Lett.*, **44**, 1417 (1980); **46**, 437 (1981).
26. Bledsoe, J. R., and Fisher, S. S., *Surf. Sci.*, **46**, 129 (1974).
27. Horne, J. M., and Miller, D. R., *Phys. Rev. Lett.*, **41** 511 (1978).
28. Armand, G., and Manson, J. R., *Surf. Sci.*, **80**, 532 (1979).
29. Bortolani, V., Franchini, A., Garcia, N., Nizzoli, F., and Santoro, G., *Phys. Rev. B.*, **28**, 7358 (1983).
30. Levi, A. C., and Suhl, H., *Surf. Sci.*, **88**, 221 (1979).
31. Feuerbacher, B., and Willis, R. F., *Phys. Rev. Lett.*, **47**, 526 (1981).
32. Ibach, H., *Chemistry and Physics of Solid Surfaces V*, Springer, Berlin, 1985, p. 455.
33. Harris, J., and Liebsch, A., *J. Phys. C*, **15**, 2275 (1982).
34. Brusdeylins, G., Rechtsheimer, R., Skofronick, J. G., Toennies, J. P., Benedek, G., and Miglio, L., *Phys. Rev. Lett.*, **54**, 466 (1985).
35. Zeppenfeld, P., Kern, K., David, R., and Comsa, G., *Phys. Rev.* **B38**, 12 329 (1988).
36. Stroscio, J. A., Persson, M., Bare, S. R., and Ho, W., *Phys. Rev. Lett.*, **54**, 1428 (1985).
37. Persson, M., Stroscio, J. A., and Ho, W., *Physica Scripta*, **36**, 548 (1987).
38. Lehwald, S., Wolf, F., Ibach, H., Hall, B. M., and Mills, D. L., *Surf. Sci.*, **192**, 131 (1987).
39. Svensson, E. C., Brockhouse, B. N., and Rowe, J. M., *Phys. Rev.*, **155**, 619 (1967).
40. Doak, R. B., Harten, U., and Toennies, J. P., *Phys. Rev. Lett.*, **51**, 578 (1983).
41. Harten, U., Toennies, J. P., and Wöll, Ch., *Faraday Discuss. Chem. Soc.*, **80**, 137 (1985).
42. Harten, U., Toennies, J. P., Wöll, Ch., and Zhang, G., *Phys. Rev. Lett.*, **55**, 2308 (1985).
43. Kern, K., David, R., Palmer, R. L., Comsa, G., and Rahman, T. S., *Phys. Rev.*, **B33**, 4334 (1986).
44. Neuhaus, D., Joo, F., and Feuerbacher, B., *Surf. Sci.*, **165**, L90 (1986).
45. Jayanthi, C. S., Bilz, H., Kress, W., and Bededek, G., *Phys. Rev. Lett.*, **59**, 795 (1987).
46. Bortolani, V., Franchini, A., Nizzoli, F., and Santoro, G., *Phys. Rev. Lett.* **52**, 429 (1984).
47. Kern, K., David, R., Palmer, R. L., Comsa, G., He, J., and Rahman, T. S., *Phys. Rev. Lett.* **56**, 2064 (1986).
48. Kern, K., David, R., Palmer, R. L., Comsa, G., and Rahman, T. S., *Surf. Sci.*, **178**, 537 (1986).
49. Neuhaus, D., Joo, F., and Feuerbacher, B., *Phys. Rev. Lett.*, **58**, 694 (1987).
50. Gibson, K. D., and Sibener, S. J., *Phys. Rev. Lett.*, **55**, 1514 (1985).
51. Kern, K., David, R., Palmer, R. L., and Comsa, G., *Phys. Rev. Lett.*, **56**, 2823 (1986).

52. Hall, B. M., Mills, D. L., and Black, J., *Phys. Rev.*, **B32**, 4932 (1985).
53. Gibson, K. D., and Sibener, S. J., *Faraday Discuss. Chem. Soc.*, **80**, 203 (1985).
54. Kern, K., Zeppenfeld, P., David, R., and Comsa, G., *Phys. Rev.*, **B35**, 886 (1987), to be published.
55. Englesfield, J. E., *Prog. Surf. Sci.*, **20**, 105 (1985).
56. Heinz, K., in *Kinetics of Interface Reactions* (Ed. M. Grunze and H. J. Kreuzer), Springer, Berlin, 1987, p. 202.
57. Binnig, G., and Rohrer, H., *Phys. Blätter*, **43**, 282 (1987).
58. Sinha, S. K. (Ed.), *Ordering in Two Dimensions*, North Holland, Amsterdam, 1980.
59. Dash, J. G., and Ruvalds, J. (Eds.), *Phase Transitions in Surface Films*, Phenum, New York, 1980.
60. Kontorova, T., and Frenkel, Ya. I., *Zh. Eksp. Teor. Fiz.*, **89**, 1340 (1938).
61. Frank, F. C., and van der Merwe, J., *Proc. Roy. Soc.* A, **198**, 205 (1949).
62. Bak, P., Mukamel, D., Villain, J., and Wentowska, K., *Phys. Rev.*, **B19**, 1610 (1979).
63. Pokrovsky, V. L., and Talapov, A. L., *Sov. Phys. JETP*, **51**, 134 (1980).
64. Kern, K., David, R., Palmer, R. L., and Comsa, G., *Phys. Rev. Lett.*, **56**, 620 (1986).
65. Gordon, M. B., and Villain, J., *J. Phys.*, **C18**, 3919 (1985).
66. Kern, K., David, R., Zeppenfeld, P., Palmer, R. L., and Comsa, G., *Solid State Comm.*, **62**, 361 (1987).
67. Zeppenfeld, P., Kern, K., and Comsa, G., *Phys. Rev.* **B38**, 3918 (1988).
68. Stephens, P. W., Heiney, P. A., Birgeneau, R. J., Horn, P. M., Moncton, D. E., and Brown, G. S., *Phys. Rev.*, **B29**, 3512 (1984).
69. Abraham, F. F., Rudge, W. E., Auerbach, D. J., and Koch, S. W., *Phys. Rev. Lett.*, **52**, 445 (1984).
70. Erbil, A., Kortan, A. R., Birgenau, R. J., and Dresselhaus, M. S., *Phys. Rev.* **B28**, 6329 (1983).
71. Fain, S. C., Chinn, M. D., and Diehl, R. D., *Phys. Rev.*, **B21**, 4170 (1980); Moncton, D. E., Stephens, P. W., Birgeneau, R. J., Horn, P. M., and Brown, G. S., *Phys. Rev. Lett.*, **46**, 1533 (1981).
72. Coppersmith, S. N., Fisher, D. S., Halperin, B. I., Lee, P. A., and Brinkman, W. F., *Phys. Rev.*, **B25**, 349 (1982).
73. Haldane, F. D. M., and Villain, J., *J. Physique*, **42**, 1673 (1981).
74. Jaubert, M., Glachant, M., Bienfait, M., and Boato, G., *Phys, Rev. Lett.*, **46**, 1679 (1981).
75. Gooding, R. J., Joos, B., and Bergersen, B., *Phys. Rev.*, **B27**, 7669 (1983).
76. Kern, K., David, R., Zeppenfeld, P., and Comsa, G., *Surf. Sci.*, **195**, 353 (1988).
77. Halpin-Healy, T., and Kardar, M., *Phys. Rev.*, **B34**, 318 (1986).
78. D'Amico, K. L., Moncton, D. E., Specht, E. D., Birgeneau, R. J., Nagler, S. E., and Horn, P. M., *Phys. Rev. Lett.*, **53**, 2250 (1984).
79. Halpin-Healy, T., and Kardar, M., *Phys. Rev.*, **B31**, 1664 (1985).
80. Miller, D. R., and Horne, J. M., *Proc. III Int. Conf. Solid, Surf.* (Eds. R. Dobrozemsky *et al.*), Vienna, 1977, p. 1385.
81. Harten, U., Lahee, A. M., Toennies, J. P., and Wöll Ch., *Phys. Rev. Lett.*, **54**, 2619 (1985).
82. Takayanagi, K., and Yagi, K., *Jpn. Inst. Met.* **24**, 337 (1983).
83. Moritz, W., private communication.
84. El-Batanouny, M., Burdick, S., Martini, K. M., and Stancioff, P., *Phys. Rev. Lett.*, **58**, 2762 (1987).
85. Ercolessi, F., Bartolini, A., Garofalo, M., Parrinello, M., and Tosatti, E., *Surf. Sci.*, **189/190**, 636 (1987).

86. Peirls, R. E., *Quantum Theory of Solids*, Clarendon, Oxford, 1955.
87. Kohn, W., in *Many Body Physics* (Eds. C. Dewitt, and L. Balian), Gordon and Breach, New York, 1968, p. 353.
88. Yonehama,K., and Schmidt, L. D., *Surf. Sci.*, **25**, 238 (1971).
89. Debe, M. K., and King, D. A., *Phys. Rev. Lett.*, **39**, 708 (1977).
90. Barker, R. A., Estrup, P. J., Jona, F., and Marcus, P. M., *Solid State Commun.*, **25**, 375 (1978).
91. Walker, J. A., Debe, M. K., and King, D. A., *Surf. Sci.*, **104**, 405 (1981).
92. Lapujoulade, J., and Salanon, B., *Surf. Sci.*, **173**, L613 (1986).
93. Ernst, H. J., Hulpke, E., and Toennies, J. P., *Phys. Rev. Lett.*, **58**, 1941 (1987).
94. Mattheiss, L. F., and Hamann, D. R., *Phys. Rev.*, **B29**, 5372 (1984).
95. Holmes, M. I., and Gustafsson, T., *Phys. Rev. Lett.*, **47**, 443 (1981).
96. Wang, X. W., and Weber, W., *Phys. Rev. Lett.*, **58**, 1452 (1987).
97. Fasolino, A., Santoro, G., and Tosatti, E., *Phys. Rev. Lett.*, **44**, 1684 (1980).
98. Fu, C. L., Freeman, A. J., Wimmer, E., and Weinert, M., *Phys. Rev. Lett.*, **54**, 2261 (1985).
99. Burton, W. K., Cabrera, N., and Frank, F. C., *Phil. Trans. Roy. Soc.*, **243A**, 299 (1951).
100. Swendsen, R. W., *Phys. Rev.*, **B17**, 3710 (1978).
101. Chin, S. T., and Weeks, J. D., *Phys. Rev.*, **B14**, 4978 (1976).
102. van Beijeren, H., and Nolden, I., in *Structure and Dynamics of Surfaces* II (Eds. W. Schommers, and P. van Blanckenhagen), Springer, Berlin, 1986, p. 259.
103. Gilmer, G. H., *Science*, **208**, 4442 (1980).
104. Jackson, K. A., and Miller, C. E., *J. Crys. Growth*, **40**, 169 (1977).
105. Pavlovska, A., *J. Cryst. Growth*, **46**, 551 (1979).
106. Balibar, S., Edwards, D. O., and Laroche, C., *Phys. Rev. Lett.*, **42**, 782 (1979).
107. Avron, J. E., Balfour, L. S., Kuper, C. G., Landau, J., Lipson, S. G., and Schulman, L. S., *Phys. Rev. Lett.*, **45**, 814 (1980).
108. Balibar, S., and Castaing, B., *Surf. Sci. Rep.*, **5**, 87 (1985).
109. Verheij, L. K., Lux, J., and Poelsema, B., *Surf. Sci.*, **144**, 385 (1984), and references therein.
110. Lapujoulade, J., Perreau, J., and Kara, A., *Surf. Sci.*, **129**, 59 (1983).
111. Idiodi, J., Bartolani, V., Franchini, A., and Santaro, G., *Phys. Rev.*, **B35**, 6029 (1987).
112. Lapujoulade, J., *Surf. Sci.*, **178**, 406 (1986).
113. Conrad, E. H., Aten, R. M., Kaufman, D. S., Allen, L. R., Engel, T., den Nijs, M., and Riedel, E. K., *J. Chem. Phys.*, **84**, 1015 (1986); **E85**, 4657 (1986).
114. Fabre, F., Gorse, D., Lapujoulade, J., and Salanon, B., *Europhys. Lett.*, **3**, 737 (1987).
115. den Nijs, M., Riedel, E. K., Conrad, E. H., and Engel, T., *Phys. Rev. Lett.*, **55**, 1689 (1985); **E57**, 1279 (1986).
116. Villain, J., Grempel, D. R., and Lapujoulade, J., *J. Phys.*, **F15**, 809 (1985).
117. Conrad, E. H., Allen, L. R., Blanchard, D. L., and Engel, T., *Surf. Sci.*, **187**, 265 (1987).
118. Williams, R. S., Wehner, P. S., Stöhr, J., and Shirley, D. A., *Phys. Rev. Lett.*, **39**, 302 (1977).
119. Fauster, Th., Schneider, R., Dürr, H., Engelmann, G., and Taglauer, E., *Surf. Sci.*, **189/190**, 610 (1987).
120. Mochrie, S. G. J., *Phys. Rev. Lett.*, **59**, 304 (1987).
121. Zeppenfeld, P., Kern, K., David, R., and Comsa, G., *Phys. Rev. Lett.* **62**, 63 (1989).